Global Biogeochemical Cycles

RESEARCH ARTICLE
10.1029/2024GB008188

A Comprehensive Analysis of Air-Sea CO_2 Flux Uncertainties Constructed From Surface Ocean Data Products

Daniel J. Ford[1], Josh Blannin[1,2], Jennifer Watts[1], Andrew J. Watson[3], Peter Landschützer[4], Annika Jersild[5,6,7], and Jamie D. Shutler[1]

[1]Department of Earth and Environmental Science, University of Exeter, Cornwall, UK, [2]Now at Met Office, Exeter, UK, [3]Global Systems Institute, University of Exeter, Devon, UK, [4]Flanders Marine Institute (VLIZ), Ostend, Belgium, [5]Max Planck Institute for Meteorology, Hamburg, Germany, [6]Now at NASA Goddard Space Flight Center, Global Modelling and Assimilation Office (GMAO), Greenbelt, MD, USA, [7]Now at Earth System Science Interdisciplinary Center, University of Maryland, College Park, MD, USA

Abstract Increasing anthropogenic CO_2 emissions to the atmosphere are partially sequestered into the global oceans through the air-sea exchange of CO_2 and its subsequent movement to depth, commonly referred to as the global ocean carbon sink. Quantifying this ocean carbon sink provides a key component for closing the global carbon budget, which is used to inform and guide policy decisions. These estimates are typically accompanied by an uncertainty budget built by selecting what are perceived as critical uncertainty components based on selective experimentation. However, there is a growing realization that these budgets are incomplete and may be underestimated, which limits their power as a constraint within global budgets. In this study, we present a methodology for quantifying spatially and temporally varying uncertainties in the air-sea CO_2 flux calculations for the fCO_2-product based assessments that allows an exhaustive assessment of all known sources of uncertainties, including decorrelation length scales between gridded measurements, and the approach follows standard uncertainty propagation methodologies. The resulting standard uncertainties are higher than previously suggested budgets, but the component contributions are largely consistent with previous work. The uncertainties presented in this study identify how the significance and importance of key components change in space and time. For an exemplar method (the UExP-FNN-U method), the work identifies that we can currently estimate the annual ocean carbon sink to a precision of ±0.70 Pg C yr^{-1} (1σ uncertainty). Because this method has been built on established uncertainty propagation and approaches, it appears that applicable to all fCO_2-product assessments of the ocean carbon sink.

Key Points:

- A framework to calculate standard uncertainty budgets for air-sea CO_2 flux data that considers all known sources of uncertainty is described
- Spatially and temporally varying air-sea CO_2 flux uncertainties, including their spatial decorrelation lengths are calculated
- For an exemplar fCO_2-product based estimate of the global ocean carbon sink, we identify a 1σ uncertainty of ±0.70 Pg C yr^{-1}

Supporting Information:

Supporting Information may be found in the online version of this article.

Correspondence to:

D. J. Ford,
d.ford@exeter.ac.uk

Citation:

Ford, D. J., Blannin, J., Watts, J., Watson, A. J., Landschützer, P., Jersild, A., & Shutler, J. D. (2024). A comprehensive analysis of air-sea CO_2 flux uncertainties constructed from surface ocean data products. *Global Biogeochemical Cycles*, *38*, e2024GB008188. https://doi.org/10.1029/2024GB008188

Received 28 MAR 2024
Accepted 9 OCT 2024

Author Contributions:

Conceptualization: Daniel J. Ford, Jennifer Watts, Andrew J. Watson, Peter Landschützer, Annika Jersild, Jamie D. Shutler
Formal analysis: Daniel J. Ford, Jamie D. Shutler
Funding acquisition: Andrew J. Watson, Jamie D. Shutler
Investigation: Daniel J. Ford
Methodology: Daniel J. Ford, Josh Blannin, Jamie D. Shutler
Project administration: Andrew J. Watson, Jamie D. Shutler
Software: Daniel J. Ford, Josh Blannin, Peter Landschützer
Supervision: Jamie D. Shutler

1. Introduction

Anthropogenic carbon dioxide (CO_2) emissions are continuing to increase and since the 1800s the ocean has acted as a net CO_2 sink helping to slow the rise in atmospheric CO_2 and the resultant global heating. This uptake equates to ~25% of all anthropogenic CO_2 emissions and is occurring at an increasing rate reaching ~2.9 Pg of carbon per year (Pg C yr^{-1}; 1 Pg C = 10^{15} g of carbon) in recent years (Friedlingstein et al., 2023). Our ability to quantify and resolve the annual uptake of CO_2 by the global oceans currently comes from primarily two sources: (a) observation fCO_2-product based assessments that extrapolate and combine sparse ocean CO_2 observations with satellite and re-analysis data into global fields through time and (b) analyses from process-based global biogeochemical models. However, other methods including atmospheric inversions are becoming more utilized (e.g., Chen et al., 2021). The fCO_2-product based assessments rely on globally complete data sets, alongside sparse in situ observations of the fugacity of CO_2 in seawater ($fCO_{2\ (sw)}$), which are collated into the annual releases of the Surface Ocean CO_2 Atlas (SOCAT) (Bakker et al., 2016). In many of these fCO_2-product based approaches, these in situ data are matched to variables such as satellite, reanalysis and model-based data of sea surface temperature (SST), salinity (SSS), mixed layer depth (MLD) and chlorophyll-*a* (Chau et al., 2022; Gregor & Gruber, 2021; Iida et al., 2021; Landschützer et al., 2014; Rodenbeck et al., 2013; Watson et al., 2020), which are used to describe the physical, biological and chemically driven variability in $fCO_{2\ (sw)}$ (Shutler et al., 2024). The relationships between these variables and $fCO_{2\ (sw)}$ are then estimated within predefined provinces or biogeochemical regions (e.g., using multi linear regressions, neural network or other machine learning techniques) to allow globally complete $fCO_{2\ (sw)}$ fields through time to be produced (Chau et al., 2022; Gregor & Gruber, 2021; Iida et al., 2021; Landschützer et al., 2016; Rodenbeck et al., 2013; Watson et al., 2020). These

Validation: Daniel J. Ford
Visualization: Daniel J. Ford
Writing – original draft: Daniel J. Ford
Writing – review & editing: Josh Blannin, Jennifer Watts, Andrew J. Watson, Peter Landschützer, Annika Jersild, Jamie D. Shutler

complete fields are then combined with a host of data including more satellite observations, model and re-analysis data sets to calculate the air-sea CO_2 fluxes, and then integrated into global or regional annual budgets (as described within Shutler et al. (2024) and used by most of the fCO_2-product based ocean sink estimates within Friedlingstein et al. (2023); and the six methods in Fay et al. (2021)).

The current uncertainty characterization of the resulting air-sea fluxes and the integrated net sink estimates from these outputs are largely based on a single estimate that is assumed constant in space or time. For example, Landschützer et al. (2014) estimated an uncertainty of ∼0.53 Pg C yr^{-1} (1 standard deviation, 1σ) for one fCO_2-product based assessment, which comprised three sources of uncertainty, though dominated mainly by one empirical parameterization used within the calculation (the gas transfer parameterization, which was assessed to contribute to ∼0.40 Pg C yr^{-1} of the uncertainty budget). Within the Global Carbon Budget (GCB) (Friedlingstein et al., 2023) uncertainties on all fCO_2-product ocean carbon sink assessments are estimated (as 1σ) using literature values for a selection of uncertainty sources including the standard deviation of the seven data product ensemble in the GCB (contributing 0.3 Pg C yr^{-1}), the $fCO_{2\ (sw)}$ mapping (contributing 0.2 Pg C yr^{-1} to the uncertainty budget) from Landschützer et al. (2014), the gas transfer coefficient (0.2 Pg C yr^{-1}) from Ho et al. (2011) and Wanninkhof et al. (2013), the wind speed data input (0.1 Pg C yr^{-1}) from Fay et al. (2021), the in situ $fCO_{2\ (sw)}$ observation uncertainty (0.2 Pg C yr^{-1}) from Wanninkhof et al. (2013) and a land to ocean river flux adjustment (0.3 Pg C yr^{-1} which unlike the other components is the 2σ value) due to natural CO_2 outgassed due to riverine material from Regnier et al. (2022). These components are assumed to be spatially and temporally independent (i.e., uncorrelated), resulting in a fixed annual standard 1σ uncertainty of ±0.6 Pg C yr^{-1}. Whilst a good first step and pragmatic solution, this approach does not systematically identify and characterize all sources of uncertainty and largely overlooks spatial correlation, which is important for some variables critical in the calculation (Watson et al., 2009). Because of this, it is likely that these estimates of the uncertainties for the fCO_2-products may be underestimated, whilst many will vary through both space and time dependent upon data coverage (Hauck, Nissen, et al., 2023) and environmental conditions. Furthermore, the apparent gradual divergence that has been observed between the model and fCO_2-product based assessments of the ocean CO_2 sink within the GCB assessments (Friedlingstein et al., 2022, 2023) may be, in part, driven by, or at least confused by, unconstrained or incomplete uncertainty budgets. Recent work by Jersild and Landschützer (2024) does provide spatially and temporally explicit uncertainties for some components of the air-sea CO_2 flux but do not systematically evaluate all known sources of uncertainty (including, for example, uncertainties in the solubility of CO_2, Schmidt number and the input temperature data set) and their approach is not generic enough to be fully applicable to all fCO_2-products within the GCB. Clearly, a full uncertainty budget for both the model and fCO_2-product based estimates is needed to support any conclusions as to which estimate is the more credible. Similarly, a more complete standard uncertainty budget would guide where to focus on efforts toward reducing these uncertainties and improving the quantification of the global ocean CO_2 sink.

Therefore, there is a desire for spatially and temporally varying uncertainties where all known sources of uncertainty are systematically evaluated into a full standard uncertainty budget. Established frameworks and methods for assessing uncertainty components exist which can be used to build standard uncertainty budgets (BIPM, 2008), which were originally developed by the metrology community, but have since seen widespread application in other scientific realms including ocean satellite remote sensing and in situ studies (e.g., Banks et al., 2020; Dong, Yang, Bakker, Kitidis, & Bell, 2021; Dong, Yang, Bakker, Liss, et al., 2021) and these use standard uncertainty propagation techniques (Taylor, 1997).

Within this study, we present a complete spatially and temporally varying air-sea CO_2 flux uncertainty budget applicable to the fCO_2-product estimates, which systematically assesses all known sources of uncertainty and propagates these using standard techniques (e.g., Taylor, 1997 and Monte Carlo methods). To complement the baseline air-sea CO_2 flux uncertainty budget, we also developed an approach to estimate spatially and temporally complete $fCO_{2\ (sw)}$ uncertainties. For a single exemplar feed forward neural network interpolation approach, we consider three sources of uncertainty that feed into the $fCO_{2\ (sw)}$ uncertainty. We highlight how the uncertainty approach for the interpolated fields can be adapted to other fCO_2-product based approaches which use different interpolation methods. The resulting air-sea CO_2 flux uncertainties are then globally integrated to produce an annual global time varying uncertainty budget for the net air-sea CO_2 flux, or ocean CO_2 sink, and the dominant components within this uncertainty budget are assessed. These results are discussed in the context of the GCB global ocean CO_2 sink uncertainty estimates, but the methods can also be applied regionally. The uncertainty approach for the complete air-sea CO_2 fluxes and the integrated net sink values are applicable to any of the fCO_2-

Table 1
Input Parameters Used Within the University of Exeter Physics Feed Forward Neural Network (UExP-FNN-U) as Predictor Variables With Their Respective Uncertainties Used Within the Parameter Uncertainty

Predictor variables	Defined 2σ uncertainty	Reference
NOAA-GML $xCO_{2\ (atm)}$	0.4 ppm	Lan et al. (2023)
CCI Sea Surface Temperature (v2.1)	0.35 K (mean uncertainty)	Merchant et al. (2019)
CMEMS sea surface salinity (GLORYS12V1)	0.2 psu	Jean-Michel et al. (2021)
CMEMS mixed layer depth (GLORYS12V1; $\log_{10}$ transformed)	0.1 $\log_{10}$(m)	Jean-Michel et al. (2021)

products. Throughout this study, the uncertainties are presented as standard deviations of a normal distribution (consistent with the GCB, and previous uncertainty assessments).

2. Methods

2.1. Input Data Sets

In situ monthly 1° gridded SOCAT2023 $fCO_{2\ (sw)}$ observations which have been reanalyzed to the depth consistent temperature CCI-SST v2.1 (Merchant et al., 2019) data set were downloaded from Ford et al. (2023). Data were extracted for the period 1985 to 2022. Following the recommendations of Shutler et al. (2024), all satellite or re-analysis data choices focussed on climate data to ensure long-term data stability and the availability of uncertainty data. Satellite or reanalysis data sets were retrieved from their respective sources at their native temporal and spatial resolution (see Table S1 in Supporting Information S1 for all the data sets used within this study) and averaged to the same monthly 1° global grid as the SOCAT observations. Some data sets did not cover the full temporal period and these periods were filled with a 10 years climatological monthly mean from the respective end of the timeseries (i.e., if missing data occurred at the start of the timeseries, a 10 years monthly climatology from the start of the available data was constructed). Anomalies for each variable were calculated with respect to a monthly climatology between 1985 and 2022. The GCB (Friedlingstein et al., 2023) version of the UoEx-Watson product was retrieved from Hauck, Landschützer et al. (2023).

The CCI-SST and EUMETSAT Ocean and Sea Ice Satellite Application Facility (OSISAF) sea ice concentrations were retrieved with a daily coincident 1σ uncertainty field. The uncertainties within these data are correlated spatially to around 100–300 km and 3 days temporally (Kern, 2021); therefore, we assumed that the uncertainties are correlated within these scales when producing the monthly 1° uncertainties, and convert to 2σ equivalent uncertainties. Uncertainties within the Copernicus Marine service (CMEMS) GLORYS12V1 salinity have been estimated with a root mean square difference (RMSD) of ∼0.3 psu (1σ) for individual daily observations (Jean-Michel et al., 2021). Similarly the Cross Calibrated Multi-Platform (CCMP) wind speeds have a RMSD of ∼0.9 ms^{-1} (1σ) for the 6 hourly observations (Mears et al., 2022a). These uncertainties were converted to the 2σ equivalents and propagated to monthly uncertainties assuming the same temporal correlations as the CCI-SST and OSISAF data. This resulted in a 0.2 psu salinity and 0.9 ms^{-1} wind speed 2σ uncertainty. Uncertainties in the atmospheric dry mixing ratio of CO_2 ($xCO_{2\ (atm)}$) were estimated as the mean of the National Oceanic and Atmospheric Administration Global Monitoring Laboratory (NOAA-GML) provided uncertainties (1σ) between 1985 and 2022 and converted to 2σ equivalents resulting in a 0.4 ppm uncertainty (Table 1).

2.2. Air-Sea CO_2 Fluxes

The air-sea CO_2 flux calculations were carried out using the open source FluxEngine toolbox (Holding et al., 2019; Shutler et al., 2016), which provides traceable, consistent, and configurable air-sea CO_2 flux calculations. The air-sea CO_2 flux (F) can be expressed in a bulk parameterization as

$$F = K_{600}\left(\mathrm{Sc}/600\right)^{-0.5}\left(\alpha_{\mathrm{subskin}} fCO_{2\ (\mathrm{sw,subskin})} - \alpha_{\mathrm{skin}} fCO_{2\ (\mathrm{atm})}\right)(1-\mathrm{ice}) \quad (1)$$

Which is consistent with the rapid model of Woolf et al. (2016) and where K_{600} is the gas transfer coefficient estimated using the Nightingale et al. (2000) parameterization and wind speeds from the CCMP (v3.1) (Mears

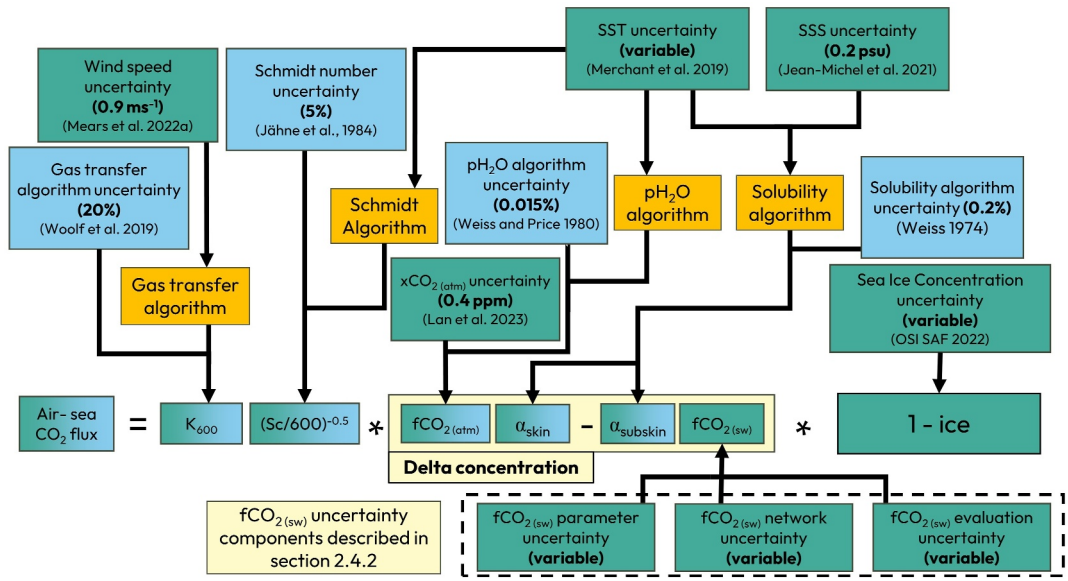

Figure 1. Flowchart indicating the sources of uncertainty (2σ) that contribute to each term in the air-sea CO_2 flux calculation described in Section 2.2 and integrated in Section 2.5. Green boxes indicate a component that decorrelates over a spatial and temporal scale, blue boxes indicate globally correlated components and orange boxes indicate functions for which uncertainties are propagated using a Monte Carlo approach. Boxes with a green to blue gradient indicate that the component has both globally correlated, and spatially correlated components. The $fCO_{2\ (sw)}$ uncertainty components (grouped by the dashed line box) are described in Section 2.4.2. References within the flowchart are for the gas transfer algorithm uncertainty (Woolf et al., 2019), wind speed uncertainty (Mears et al., 2022a), Schmidt number algorithm uncertainty (Jähne et al., 1984), partial pressure of water vapor (pH_2O) algorithm (Weiss & Price, 1980), $xCO_{2\ (atm)}$ uncertainty (Lan et al., 2023), SST uncertainty (Merchant et al., 2019), SSS uncertainty (Jean-Michel et al., 2021), solubility algorithm uncertainty (Weiss, 1974) and the sea ice concentration uncertainty (OSI SAF, 2022). Acronyms in the flowchart are gas transfer coefficient (K_{600}), Schmidt number (Sc), fugacity of CO_2 in atmosphere ($fCO_{2\ (atm)}$) and seawater ($fCO_{2\ (sw)}$) and solubility at the subskin ($\alpha_{subskin}$) and skin (α_{skin}).

et al., 2022a, 2022b). Sc is the Schmidt number estimated using the calculation in Wanninkhof (2014) and the ocean's skin temperature. α is the solubility of CO_2 at the respective subskin or skin temperature and salinity, which was estimated as in Weiss (1974). $fCO_{2\ (atm)}$ and $fCO_{2\ (sw,subskin)}$ are the fugacity of CO_2 in the atmosphere and the seawater subskin layer, respectively. Equation 1 and the use of skin and subskin temperatures accounts for vertical temperature gradients across the ocean's mass boundary layer as described in Woolf et al. (2016), where we refer the reader for further information and the assignment of data to the skin and subskin quantities is described below.

For the $fCO_{2\ (sw,subskin)}$, we use complete fields generated by an exemplar neural network approach (University of Exeter Physics Feed Forward Neural Network with Uncertainties; UExP-FNN-U) described in Section 2.4. The CCI-SST and CMEMS SSS are considered representative of the subskin temperature and salinity and used in the calculation of $\alpha_{subskin}$. For the atmospheric side, the ocean's skin temperature was estimated from the CCI-SST with a cool skin deviation calculated with NOAA-COARE3.5 (Edson et al., 2013; Fairall et al., 1996; Ludovic et al., 2021) using CCMP wind speed, CCI-SST and ERA5 fields (Hersbach et al., 2019) as inputs. Skin salinity was calculated assuming a +0.1 psu change from the CMEMS SSS (i.e., a salty skin) as in Watson et al. (2020) and Woolf et al. (2019). $fCO_{2\ (atm)}$ was calculated using the NOAA-GML $xCO_{2\ (atm)}$ (Lan et al., 2023), the skin temperature and ERA5 atmospheric pressure. Sea ice concentrations from the OSISAF (OSI SAF, 2022) data set were used for the ice component of Equation 1.

2.3. Air-Sea CO_2 Flux Uncertainties

The spatially and temporally varying air-sea CO_2 flux uncertainties were calculated using a framework that assesses all identified sources of uncertainties (Figure 1). Figure 1 indicates the sources of uncertainties that contribute to the individual components of Equation 1. Uncertainties within each component were propagated through the flux calculations using standard propagation techniques (e.g., where a specific value is known) or a

Monte Carlo uncertainty propagation approach (e.g., where the component is dependent upon multiple input data or to allow future flexibility in the parameterization selection) to produce an uncertainty in the air-sea CO_2 flux due to each component (calculated at the 95% confidence).

As an example, the process for propagating the uncertainties contributing to the K_{600} uncertainty is described, where these principles apply to all components. K_{600} shows two sources of uncertainty: (a) the gas transfer parameterization uncertainty when parameterized with in situ observations, which has been indicated as ∼20% (Woolf et al., 2019) and (b) the uncertainty within the wind speed product used in driving the gas transfer parameterization. The first component can be propagated with standard propagation techniques, resulting in a 20% uncertainty (assumed to be 95% confidence) in the calculated CO_2 flux. The second wind speed uncertainty component was propagated through the gas transfer parameterization using a Monte Carlo uncertainty propagation, where the wind speed was perturbed randomly 100 times within its uncertainty (0.9 ms^{-1} where we assume this was a 95% confidence) (Mears et al., 2022a). The two standard deviations of the resulting distribution of K_{600} were calculated, converted to a percentage uncertainty, and propagated using standard techniques to a CO_2 flux uncertainty. This resulted in a spatially varying uncertainty with a global mean of ∼20%, however significantly varying regionally, ranging from 10% to greater than 100%. For a total uncertainty on K_{600} for each 1° grid cell, the two components could be combined in quadrature assuming they are independent and uncorrelated (Taylor, 1997).

This approach and principles apply to all components in Figure 1 except for the sea ice concentration and the interpolation of the fCO_2 data. The uncertainty estimate of the interpolated fCO_2 is a more specialized case which needs to capture multiple sources of uncertainty, which are the network uncertainty (standard deviation of the neural network ensemble), input parameter uncertainties (propagated input parameter uncertainties used for the interpolation) and the evaluation uncertainty (uncertainty with respect to the SOCAT observations), and the definition and approach taken for these are described in Section 2.4.2. The sea ice uncertainty contribution was not included in the total air-sea CO_2 flux uncertainty due to the asymmetric nature of the sea ice concentration when applying a Monte Carlo uncertainty propagation (i.e., the sea ice concentration cannot be less than 0% or greater than 100% and therefore the resulting uncertainty distribution after applying the Monte Carlo uncertainty propagation would become skewed). These asymmetric distributed uncertainties cannot be combined with the symmetric uncertainty distributions using standard propagation techniques (Taylor, 1997). Therefore, the sea ice concentration uncertainties are assessed within the globally integrated uncertainties described in Section 2.5.

2.4. Calculating Spatially Complete $fCO_{2\ (sw)}$ Data and Estimating Their Uncertainties

The sparse sampling of the in situ data used, the need to use an interpolation method, and the need for input data for the interpolation methods warrant a more comprehensive analysis of the fCO_2 data uncertainties. These sections now describe the interpolation technique and the approach for assessing the uncertainties for input into the framework in Figure 1.

2.4.1. The Neural Network Approach—University of Exeter Physics Feed Forward Neural Network With Uncertainties (UExP-FNN-U)

The self-organizing map feed forward neural network (SOM-FNN) method (Landschützer et al., 2014, 2016) used within the GCB UoEx-Watson product (Friedlingstein et al., 2023; Watson et al., 2020) was applied with modifications to interpolate the re-analyzed SOCAT sourced in situ fCO_2 data. These modifications were the Arctic Ocean was defined as a single province using the Longhurst province (Longhurst, 1998) Boreal Arctic (Province 1). The Mediterranean Sea and Red Sea Longhurst provinces (Province 16 and 25, respectively) were combined into a single province covering these regions, leading to a total of 18 provinces (instead of 17 as in UoEx-Watson) and near global coverage. The predictor variables remained consistent with the UoEx Watson product, consisting of SST, SSS, MLD, $xCO_{2\ (atm)}$, and anomalies of all four variables (Table 1).

These predictor variables were matched in space and time to the re-analyzed SOCAT observations (Figure 2). For each province, the SOCAT gridded $fCO_{2\ (sw)}$ observations, with their respective predictor variables, were split into two data sets: (a) an independent test data set that was not used in the neural network training or validation steps (5%) and (b) a training and validation data set (95%). These data split provides as much of the data to the neural network training, whilst retaining a sufficient sample to independently assess the neural network performance. The training and validation data set was then used within a feed forward neural network (FNN). The

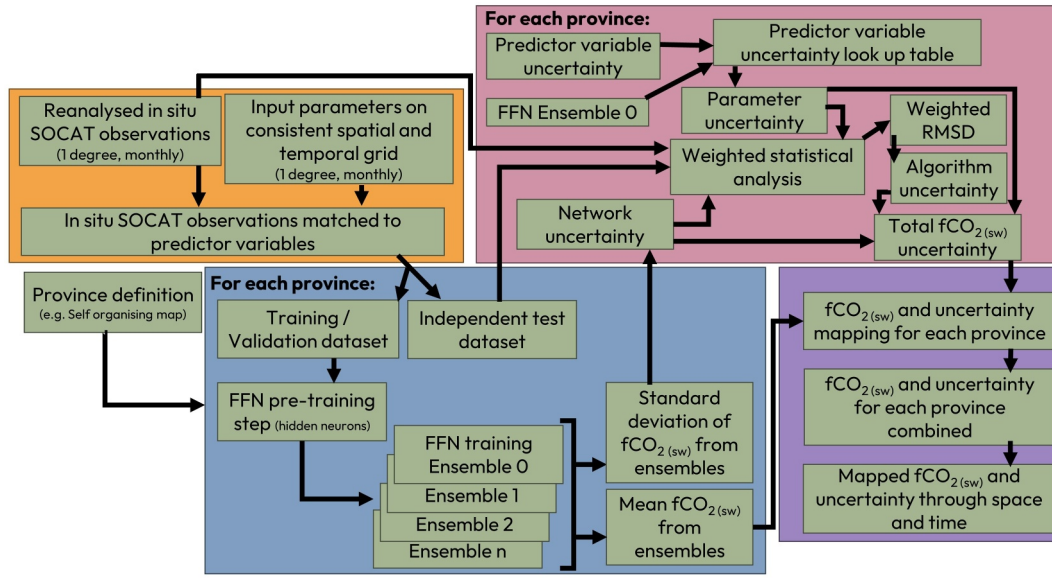

Figure 2. Flowchart indicating the structure and training scheme of the feed forward neural network approach and uncertainty analysis as described in Sections 2.4.1 and 2.4.2. Acronyms in the flowchart are Surface ocean CO_2 Atlas (SOCAT), fugacity of CO_2 in seawater ($fCO_{2\ (sw)}$), feed forward neural network (FFN) and root mean square difference (RMSD).

FFN approach consists of an input layer, hidden layer, and output layer. The input layer consists of nodes corresponding to the number of predictor variables, and a single node in the output layer. The number of nodes within the hidden layer was determined through a pre-training step (Ford et al., 2022a; Landschützer et al., 2014), which incrementally increases the hidden layer nodes in a set range (30–300 nodes at 30 increments) and finds the minimum of the neural network loss function, which corresponds to the RMSD between the neural network output and the validation component training data set. The pre-training step was required to provide the optimum number of hidden neurons to fit the in situ observations whilst preventing overfitting (Demuth et al., 2008). Once the optimum number of nodes in the hidden layer is selected, an ensemble of 10 neural networks are trained using the training and validation data set. The training and validation data set was split further and randomly into the training (70%) and validation data sets (30%) for each ensemble member. The split percentages were estimated with the optimal split approach described by Amari et al. (1997). This random splitting allows the neural network ensemble a high probability to determine all the dataset as either training or validation data. Once all ensembles have been trained, the output $fCO_{2\ (sw)}$ for the province was the mean of the ensembles. Applying this "mean" neural network for each province to the complete fields of the predictor variables allows the generation of complete and spatially complete $fCO_{2\ (sw)}$ fields (Figure 2).

2.4.2. Spatial and Temporally Varying $fCO_{2\ (sw)}$ Uncertainty Determination

The characterization of uncertainties in the $fCO_{2\ (sw)}$ neural network approach applied here allows the determination of spatially and temporally varying uncertainties in the estimated $fCO_{2\ (sw)}$. Three sources of uncertainty in the neural network $fCO_{2\ (sw)}$ are considered (and shown in Figure 2 in detail) and these are analyzed and then included within the air-sea CO_2 flux uncertainties framework within Figure 1 (see the three boxes that are grouped by a dashed line in the bottom right of Figure 1).

The first uncertainty component consists of the neural network uncertainty, whereby the random nature of the neural network approaches can lead to different optimum outcomes of a single network. This uncertainty was assessed as two standard deviations (2σ) of 10 neural network ensemble runs described in Section 2.4.1, thereby providing the mean and standard deviation of the ensembles on a per pixel basis. Regions where the 2σ value is small indicate where the neural network ensembles are well constrained with different training and validation splits, and thus output similar $fCO_{2\ (sw)}$ estimates with low variability between estimates. The first ensemble member is also used within the second uncertainty component of the $fCO_{2\ (sw)}$.

The second uncertainty component considered is the impact of the uncertainties in the predictor variables on the resulting interpolated fields, as described in Ford et al. (2021), and applied to $fCO_{2\ (sw)}$ in Ford et al. (2022a). The uncertainties in the predictor variables were propagated through the first neural network ensemble (for practical reasons, this analysis was only applied to the first member of the ensemble described above due to the computational load). In summary, an n-dimensional (n being the number of predictor variables) linear spaced grid was constructed between the maximum and minimum of each predictor variable. The linear spacing was determined such that the total number of grid points does not exceed a defined value (whereby increasing this number increases the resolution of the grid but increases computation). At each point in the grid, the predictor variables were randomly perturbed within their uncertainty (Table 1; assuming these are 95% confidence) and the $fCO_{2\ (sw)}$ was estimated for each perturbation. The two standard deviations of the resulting $fCO_{2\ (sw)}$ distribution were taken as the input parameter uncertainty (2σ uncertainty). The process is repeated for every combination in the n-dimensional grid. This grid became a look-up table for the input parameter uncertainty on the $fCO_{2\ (sw)}$ using linear interpolation between grid points. Thus, allowing the determination of the input parameter uncertainty at any combination of input variables in a computationally efficient setup.

The third uncertainty component considered was the evaluation uncertainty, or how accurate and precise the neural network estimates of the $fCO_{2\ (sw)}$ are with respect to the in situ gridded SOCAT observations. For each province, the independent test observations are compared to the neural network ensemble mean using a weighted statistical analysis as described in Ford et al. (2021). The weighting procedure allows both uncertainties in the neural network and the in situ data to be included in the assessment of the evaluation uncertainty. The neural network uncertainty for the weighting was determined as the network and input parameter uncertainties combined in quadrature (Taylor, 1997), consistent with Ford et al. (2021). The in situ observation uncertainty was calculated as the standard error of the in situ SOCAT observations in a particular grid cell combined in quadrature with an assumed measurement uncertainty of 5 µatm (Bakker et al., 2016; Taylor, 1997) (so information from the two previously described uncertainty components are used within the derivation of this third component). The standard error was used, instead of the standard deviation as in previous work (e.g., Ford et al., 2022a), as in theory the higher the number of observations within a grid cell then the higher the confidence that the mean of these will correspond to the "true" $fCO_{2\ (sw)}$. The weighted statistical analysis provides the bias (accuracy), RMSD (precision), along with the slope and intercept of a type II linear regression and the number of observations. The neural network approaches generally have a bias (accuracy) near ∼0 µatm indicating a high accuracy; however, the RMSD (precision) is generally larger (values closer to ∼0 indicate a higher precision) (Ford et al., 2022a; Gregor et al., 2019; Landschützer et al., 2014). For each province, the weighted RMSD multiplied by two (2σ, 95% confidence uncertainty) was taken as the combined algorithm uncertainty, and the bias assumed to be negligible (i.e., maximum biases are ∼10% of the corresponding RMSD) compared to the RMSD (example per province scatter plots shown in Figure S1 of the Supporting Information S1). The multiplication of the RMSD by two to achieve a 2σ uncertainty is justified within Figure S1 in Supporting Information S1.

Once all three components are calculated, they are combined in quadrature (Taylor, 1997) to provide the total uncertainty on the $fCO_{2\ (sw)}$. The three uncertainty components are all calculated or applied during the mapping procedure to produce complete fields of $fCO_{2\ (sw)}$ with a concurrent total uncertainty (considered a 2σ; 95% confidence uncertainty). The structure of neural networks commonly referred to as a structural uncertainty (i.e., hidden node number selection or province definition) will affect all three components of $fCO_{2\ (sw)}$ uncertainty and therefore is implicitly included in the uncertainty budget.

2.5. Integrated Air-Sea CO_2 Fluxes and Uncertainties

The monthly air-sea CO_2 fluxes and their uncertainties can be used to construct annual global budgets of the net CO_2 flux. The area of each pixel was calculated assuming that the Earth is an ellipsoid, and high resolution land percentage masks were produced from the General Bathymetric Chart of the Oceans (GEBCO) bathymetry data (GEBCO Bathymetric Compilation Group, 2023). The high resolution approach ensures that coastal region contours are well captured to avoid unnecessary precision or rounding errors (as described by Shutler et al. (2016)). The calculated CO_2 fluxes (g C m^{-2} d^{-1}) are multiplied by the pixel area (m^2), land percentage masks, and the days within each month and then summed into annual CO_2 fluxes (Pg C yr^{-1}). The annual absolute air-sea CO_2 flux was also calculated (i.e., $|F|$, the absolute air-sea CO_2 flux from Equation 1 regardless of whether into or out of the ocean).

The integration of the air-sea CO_2 flux uncertainties within the uncertainty budget must be treated carefully (Figure 1). In general, most components within the air-sea CO_2 flux calculations have a systematic component that will be correlated globally (Figure 1; blue boxes) and a component that will be correlated to a spatial and temporal scale (Figure 1; green boxes). Following standard geostatistical methods, these two components (correlated globally and correlated to a spatial/temporal scale) must be treated differently when integrating globally (see the Supplementary of Watson et al. (2009)). The globally correlated components (Figure 1; blue boxes) can be integrated in the same way as the air-sea CO_2 fluxes. Therefore, the CO_2 flux uncertainty (g C m^{-2} d^{-1}) at each pixel location was first multiplied by the area of the pixel (m^2), land percentage mask and the number of days in the month, and then summed into an annual CO_2 flux uncertainty for each systematic component (Pg C yr^{-1}). The procedure for globally integrating the uncertainty component that correlates to a spatial and temporal scale (Figure 1; green boxes) requires an understanding of the scales at which spatial features, and therefore their associated uncertainties, decorrelate. It was first assumed that the uncertainties are not correlated between months (i.e., no temporal correlation) as previous work shows that for the SST (from the CCI-SST data) and sea ice concentrations (from the OSISAF data) the uncertainties correlate up to period of only a few days (Kern, 2021). The spatial decorrelation length for each component (Figure 1; green boxes) was assessed using a semi-variogram approach, as used in previous studies (Landschützer et al., 2013, 2014; Watson et al., 2009). The analysis calculates the semi-variance within the uncertainty field at point-to-point Haversine (great circle) distances and estimates the "range," or the distance at which the semi-variance does not change. The range indicates the distance within which the uncertainties can be deemed to be correlated.

The following methods are consistent with the variogram analysis used for air-sea CO_2 gas fluxes by Watson et al. (2009) and Landschützer et al. (2013, 2014). The semi-variogram analysis was implemented using SciKit-GStat v1.0 (Mälicke, 2022) parameterized with the Dowd semi-variance estimator and fitted to an exponential variogram model. The semi-variogram was fitted to a random subsample of 200 points extracted from each month's uncertainty fields and repeated 100 times. The monthly perturbations were combined into an annual distribution (∼1,200 perturbations) and the median and interquartile range extracted from the distribution (example histograms for SST shown in Figure S2 of the Supporting Information S1). In cases where a monthly uncertainty field had less than 200 points, the subsample was constructed on the number of available points divided by two.

The uncertainty fields supplied to the semi variogram analysis fell into three categories: (1) a complete uncertainty field, (2) incomplete residual fields between the parameter and in situ observations, or (3) complete residual fields between two data sets for the parameter. The SST (CCI-SST), and sea ice concentration (OSISAF) and $fCO_{2\ (sw)}$ network uncertainties (Figure 1) had full uncertainty fields (category 1), which were applied to the semi variogram analysis indicating median decorrelation lengths of ∼1,300, ∼1,500, and ∼1,800 km, respectively, between 1985 and 2022. Although complete uncertainty fields were available for $fCO_{2\ (sw)}$ parameter and evaluation, these fields have non-continuous values resulting in a lack of convergence for the semi-variogram analysis (i.e., the methodological decisions in Section 2.4.2 cause these fields to be roughly single values for each province). Therefore, for the $fCO_{2\ (sw)}$ evaluation and parameter uncertainties, we have to use an incomplete uncertainty field (category 2 field) to estimate the decorrelation lengths. The residuals between the in situ monthly SOCAT $fCO_{2\ (sw)}$ observations and the neural network ensemble mean are mapped (category 2) and supplied to the semi-variogram approach. This gave a median decorrelation length of ∼2,400 km. The wind speed uncertainty presents no complete uncertainty field or in situ observations; therefore, we assess the spatial residual variability between two different wind speed data sets, CCMP v3.1 and ERA5 wind speeds (category 3), as an estimate of the decorrelation lengths. This analysis estimated a median decorrelation length of ∼4,000 km. Finally, for $xCO_{2\ (atm)}$ we assign a decorrelation length of 2,000 ± 1,500 km estimated using the global locations of the in situ stations that supply data to the NOAA-GML product, and for SSS we assume the uncertainty decorrelated at the same spatial scale as the CCI-SST (∼1,300 km). The calculated decorrelation lengths varied in time and had their respective uncertainties.

These decorrelation lengths have previously been used to estimate the number of decorrelated areas within a region, either globally (Landschützer et al., 2014) or regionally (Landschützer et al., 2013; Watson et al., 2009). The number of decorrelated regions is then combined with a spatially fixed uncertainty to estimate the integrated uncertainty. However, in this study, we have estimated spatially varying uncertainty fields which cannot be applied to the methodology of the previous studies. We therefore integrate the uncertainty component that

correlates with a spatial scale using the calculated decorrelation lengths and spatially varying uncertainty fields within a Monte Carlo uncertainty propagation.

In summary, a global grid of points was calculated where each point was separated by twice the decorrelation length for the component being calculated. At each point, a random value between −1 and 1 was assigned. These values were then linearly interpolated onto the same 1° global grid as the air-sea CO_2 flux data, such that each global 1° location has a value between −1 and 1 assigned. This was repeated for each month in the timeseries between 1985 and 2022, producing a global grid of perturbation values through time. This perturbation grid has systematic spatial structures (of values between −1 and 1) that are consistent with the decorrelation length scale, and therefore the number of decorrelated areas in previous studies (Landschützer et al., 2014; Watson et al., 2009). The complete space time fields of the air-sea CO_2 flux uncertainty were multiplied by the perturbation values and added to the calculated air-sea CO_2 flux. The annual net CO_2 flux budget calculations described at the start of Section 2.5 were conducted on the perturbed air-sea CO_2 fluxes. This process was repeated 100 times (results converged at ∼50 ensembles, and no change was found over 100 ensembles) with the decorrelation length perturbed randomly within its uncertainty at the start of each ensemble. The two standard deviations of the resulting 100 ensembles of annual net CO_2 fluxes were taken as the globally integrated uncertainty of the component.

To provide confidence in our Monte Carlo uncertainty propagation methodology, we replicate the global integrated $fCO_{2\ (sw)}$ uncertainty presented in Landschützer et al. (2014) of ∼0.18 Pg C yr^{-1} (1σ) for the period 1998 to 2010. Here we supply the calculated decorrelation lengths for the $fCO_{2\ (sw)}$ evaluation uncertainty in this study, as our neural network approach is based on the Landschützer et al. (2014) methodology, and a fixed $fCO_{2\ (sw)}$ evaluation uncertainty of 12 μatm (1σ). With these inputs, the Monte Carlo uncertainty propagation estimates a 1σ uncertainty of ∼0.20 Pg C yr^{-1} for the period 1998 to 2010, which is within 10% of, and consistent with, the Landschützer et al. (2014) result.

The integrated uncertainty components were calculated at the 95% confidence (or equivalent to a 2σ uncertainty), but to enable comparisons to the GCB values (Friedlingstein et al., 2023), we also expressed these at 1σ.

2.6. Limitations

Within this study, the uncertainties have an inherent assumption of unbiased, non-skewed Gaussian uncertainties such that the standard deviation represents the full uncertainty characteristics. For input data sets such as the CCI-SST (Merchant et al., 2019), the uncertainties are provided as standard deviations of a normal distribution and therefore, we can assume no bias or skew. For literature sources, information on the bias or skew are generally not reported, and therefore, the assumption must be made that they are unbiased and non-skewed. This would not appear as a major limitation of this study as the focus was on the precision of the air-sea CO_2 flux, whereby any bias in the underlying data would likely not affect the precision but only the accuracy. If, in the future, significant bias or skew were identified, the Taylor uncertainty propagation (Taylor, 1997) would not feasibly capture this information, and alternative propagation techniques such as Monte Carlo uncertainty propagation can be implemented (already used in cases where a potential skew has been identified in the sea ice uncertainty). Here we provide a robust foundation for data product based uncertainty estimates that can be built upon for more detailed analyses into data skewness; for example, Woolf et al. (2019) used bootstrapping to investigate the effect of individual cruise lines from the SOCAT data set on the resulting interpolated $fCO_{2\ (sw)}$.

The gridding of the SOCAT $fCO_{2\ (sw)}$ observations onto a regular 1° monthly grid will also introduce a source of uncertainty. Gregor and Gruber (2021) estimate a representation uncertainty of ∼7 μatm (1σ) for the open ocean from a limited number of locations with sufficient data to evaluate this uncertainty component. We are unable to calculate a spatially and temporally varying representation error to include within our approach. However, as highlighted in Gregor and Gruber (2021), this component was smaller than their predication uncertainty (which is equivalent to the $fCO_{2\ (sw)}$ evaluation and parameter uncertainties in this study) and therefore we do not see this as a major limitation.

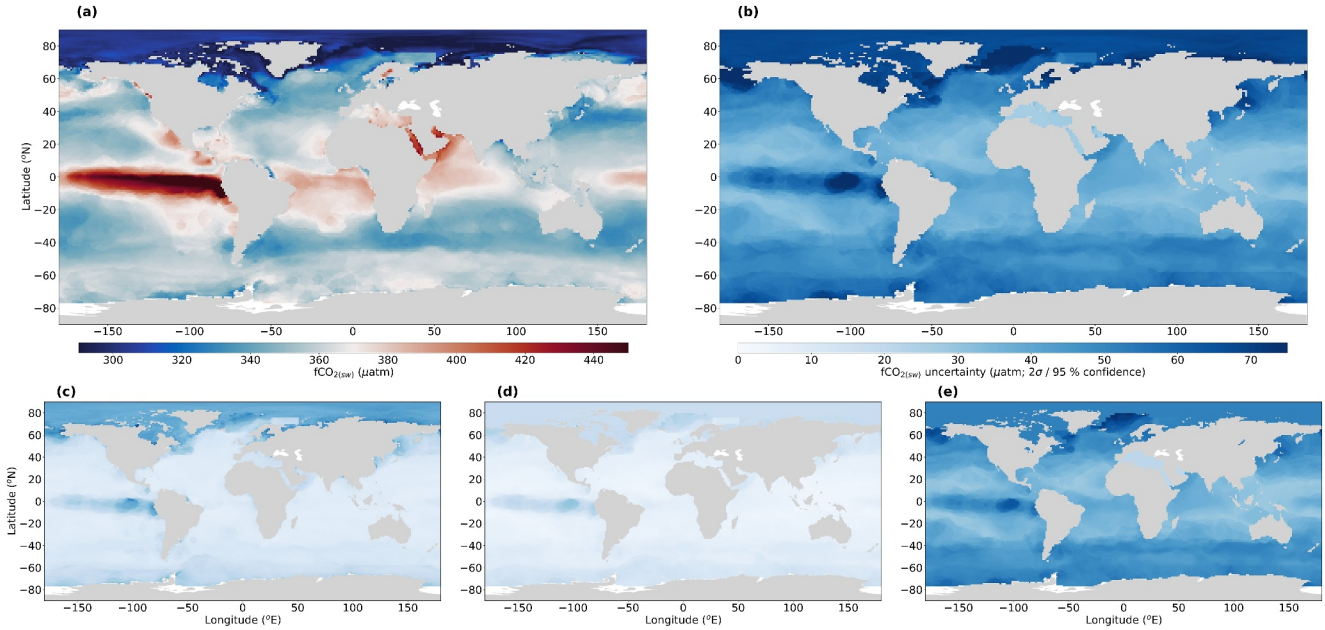

Figure 3. (a) Global mean $fCO_{2\ (sw)}$ between 1985 and 2022 where the colorbar is centered on the mean atmospheric CO_2 concentration for the same period. (b) Global mean total $fCO_{2\ (sw)}$ 2σ uncertainty between 1985 and 2022. Panel (c) same as (b) but for the $fCO_{2\ (sw)}$ network uncertainty. Panel (d) same as (b) but for the $fCO_{2\ (sw)}$ parameter uncertainty. Panel (e) same as (b) but for the $fCO_{2\ (sw)}$ evaluation uncertainty. Note (c–e) are plotted on the same colorbar as (b).

3. Results

3.1. $fCO_{2\ (sw)}$ 2σ Uncertainties

The UExP-FNN-U estimated mean $fCO_{2\ (sw)}$ between 1985 and 2022 showed global spatial variability consistent with the UoEx-Watson data product but with extended coverage into the Arctic Ocean and Mediterranean Sea (Figure S3 in Supporting Information S1; Figure 3a). The concurrent mean total $fCO_{2\ (sw)}$ 2σ uncertainty estimated from the neural network showed a mean value of ∼45 µatm, with clear geographical differences (Figure 3b). The subtropics generally showed lower uncertainties around ∼25 µatm, whereas larger uncertainties were prevalent in the Arctic Ocean, Southern Ocean and Equatorial Pacific with values greater than 50 µatm.

The dominant component driving the total $fCO_{2\ (sw)}$ 2σ uncertainty varied spatially (Figures 3c–3e). The $fCO_{2\ (sw)}$ parameter uncertainty showed consistently lower values ranging from 2 µatm up to maxima at ∼15 µatm (Figure 3d). Maxima generally occurred in dynamic regions including the Arctic and Equatorial Pacific; however, the parameter uncertainty was not a dominant source of the total uncertainty. The network uncertainty indicated minima around ∼10 µatm which occurred in the subtropics and increased to maxima greater than ∼50 µatm in the Arctic Ocean (Figure 3c). The evaluation uncertainty ranged from ∼20 µatm in the subtropics and Mediterranean Sea up to maxima ∼70 µatm in the polar North Atlantic Ocean (Figure 3e). The evaluation uncertainty was generally the dominant component in the subtropics and the polar North Atlantic, whereas the network uncertainty was the dominant component in some regions of the Arctic Ocean and Equatorial Pacific (Figures 3c and 3e).

3.2. Air-Sea CO_2 Flux Uncertainties

The mean total air-sea CO_2 flux 2σ uncertainties between 1985 and 2022 showed minima around ∼0.01 g C m^{-2} d^{-1} in the subtropics to maxima greater than 0.2 g C m^{-2} d^{-1} in the polar oceans (Figure 4a). In all regions, the total $fCO_{2\ (sw)}$ uncertainty was the dominant component, with relative contributions ranging from 60% to 75% (Figures 4b–4e; Bar 0). In most regions, the next largest components to the uncertainty generally stem from the gas transfer parameterization and the wind speed uncertainties, which are the dominant inputs to the gas transfer calculation (Figures 4b–4e; Bar 1; Figure S4 in Supporting Information S1). In the Southern Ocean, the gas transfer parameterization uncertainty was larger with relative contributions greater than 50% compared to the wind speed uncertainty (Figure 4e; Bar 2). In the polar North Atlantic, the gas transfer parameterization and wind

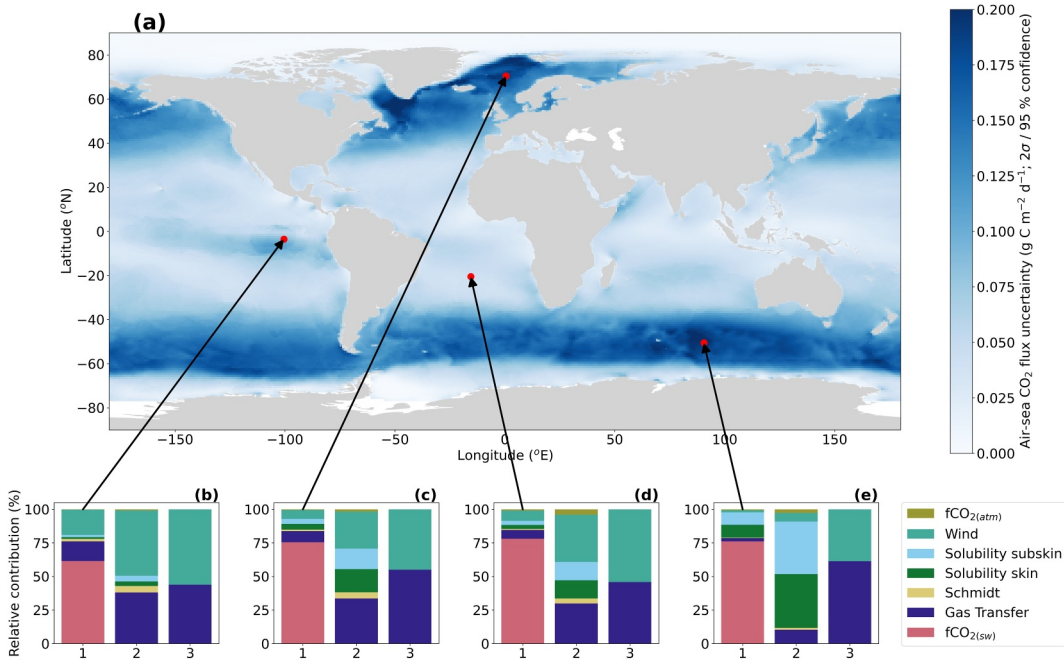

Figure 4. (a) Global mean air-sea CO_2 flux 2σ uncertainty between 1985 and 2022. (b) Mean relative contribution bar chart for each of the air-sea CO_2 flux uncertainty components between 1985 and 2022 at the highlighted location. Bar 1 shows all labeled sources of uncertainty. Bar 2 shows the contributions for all components removing the $fCO_{2\,(sw)}$ component. Bar 3 shows the relative contribution for the wind speed and gas transfer components. Panels (c–e) same as (b) but for the respective points highlighted.

speed both contributed the same (Figure 4c; Bar 2). However, in the subtropical South Atlantic and Equatorial Pacific, the wind speed uncertainty was larger than the gas transfer parameterization component (Figures 4a and 4d; Bar 2; Figure S4 in Supporting Information S1). The remaining uncertainty components, including the $fCO_{2\,(atm)}$, air and waterside solubilities and Schmidt number, were generally smaller components with relative contributions totaling to around 5% of the total uncertainty (Figures 4b–4d; Bar 0). However, in the Southern Ocean, the air and waterside solubility components accounted for ∼20% of the total uncertainty and were larger than the gas transfer and wind components (Figure 4e; Bar 0).

3.3. Integrated Net Air-Sea CO_2 Flux and 1σ Uncertainties

The globally integrated net air-sea CO_2 flux indicated a net CO_2 sink of ∼2.2 Pg C yr^{-1} between 1985 and 1995 before reducing to a minimum in 2000 of ∼2.0 Pg C yr^{-1}. There after the CO_2 sink increased steadily from ∼2.0 Pg C yr^{-1} in 2002 to ∼3.4 Pg C yr^{-1} in 2020 (Figure 5d). The evolution of the CO_2 sink estimated by this UExP-FNN-U analysis is consistent with that of the UoEx-Watson product (Figure 5d). The 1σ total integrated CO_2 flux uncertainty had a mean of ∼0.70 Pg C yr^{-1} between 1985 and 2022, ranging from a minimum of ∼0.60 Pg C yr^{-1} around 2000 to a maximum of ∼0.82 Pg C yr^{-1} in 2022 (Figure 5d; Table 2).

The dominant components contributing to the total uncertainty changed over the period 1985 to 2022 (Figure 5a, Figure S5a in Supporting Information S1). Between 1985 and 2000, the $fCO_{2\,(sw)}$ uncertainty decreased from ∼0.65 to ∼0.45 Pg C yr^{-1} but remained the dominant component in this period. During the period 2001 to 2022, the $fCO_{2\,(sw)}$ and gas transfer uncertainties show relatively equal contributions to the total uncertainty of ∼0.49 Pg C yr^{-1}. However after ∼2010 the gas transfer uncertainties were marginally more dominant. The $fCO_{2\,(sw)}$ uncertainty was made up of the three sources of neural network uncertainty (Figure 5b). The parameter uncertainty showed the lowest contribution of ∼10%, whereas the evaluation and network uncertainties had contributions of 6% and 30% respectively. But these contributions changed through time, whereby the evaluation uncertainty contribution was generally higher at the start and end of the timeseries, with minima around 1997. The network uncertainty showed a reciprocal change to that of the evaluation uncertainty, whereas the parameter uncertainty stayed relatively constant through time.

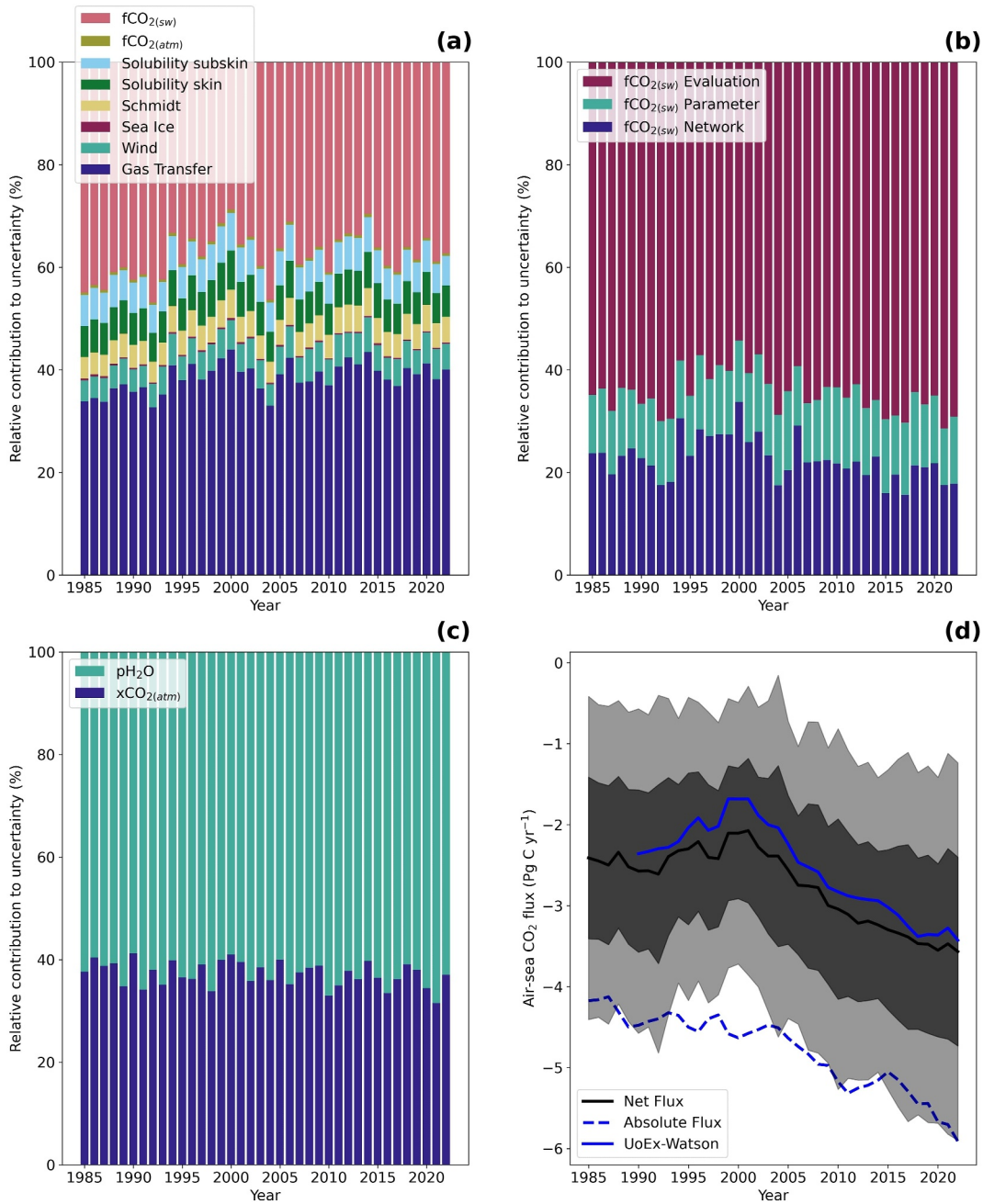

Figure 5. (a) Mean relative contributions between 1985 and 2022 for each uncertainty component to the globally integrated air-sea CO_2 flux. Panel (b) same as (a) but for the three $fCO_{2\ (sw)}$ uncertainty components that contribute to the total $fCO_{2\ (sw)}$ in (a). Panel (c) same as (b) but for the two uncertainty components that contribute to the $fCO_{2\ (atm)}$ in (a). (d) Net air-sea CO_2 flux calculated between 1985 and 2022 (black line). The dark gray region indicates the 1σ and the light gray region indicates the 2σ total air-sea CO_2 flux uncertainty. Blue dashed line indicates the absolute air-sea CO_2 flux (i.e., the integrated absolute CO_2 flux across the air-sea interface). Blue line indicates the UoEx-Watson product from the Global Carbon Budget 2023 (Friedlingstein et al., 2023). Absolute contributions are shown in Figure S5 of the Supporting Information S1.

The gas transfer parameterization uncertainty was the next dominant component of uncertainty after the $fCO_{2\ (sw)}$ increase from 0.40 Pg C yr^{-1} in 1985 to 0.58 Pg C yr^{-1} in 2022 (Figure 5a, Figure S5 in Supporting Information S1). This increase largely followed the increase in the absolute air-sea CO_2 flux, from 4 Pg C yr^{-1} in 1985 to 5.8 Pg C yr^{-1} in 2022 (Figure 5d). After ~2010 the gas transfer parameterization became the marginally more

Table 2
Mean 1σ Uncertainty Between 1985 and 2022 for Each Component

Component	Mean 1σ uncertainty between 1985 and 2022 (Pg C yr^{-1})	Mean fixed component contribution (Pg C yr^{-1})	Mean spatially varying component (Pg C yr^{-1})
Gas transfer	0.47	0.47	N/A
Wind	0.07	N/A	0.07
Sea ice	0.003	N/A	0.003
Schmidt	0.06	0.06	0.001
Solubility skin	0.08	0.08	0.02
Solubility subskin	0.07	0.07	0.02
$fCO_{2\ (atm)}$	0.006	0.005	0.003
$fCO_{2\ (sw)}$	0.48	N/A	0.48
Total	0.70		

Note. These mean uncertainty can be split into a fixed (globally correlated) component and a component that was correlated to a spatial and temporal period. The total mean uncertainty between 1985 and 2022 assuming the uncertainties are independent and uncorrelated (Taylor, 1997) is shown in the total row. Equivalent 2σ uncertainties shown in Table S2 of the Supporting Information S1.

dominant source of uncertainty, and before this period, the $fCO_{2\ (sw)}$ remained the dominant source of uncertainty. The other components showed lower contributions to the total uncertainty with mean contributions between 1985 and 2022 of 0.07 Pg C yr^{-1} for the wind speed, 0.08 Pg C yr^{-1} for the solubility components, 0.06 Pg C yr^{-1} for the Schmidt number, 0.006 Pg C yr^{-1} for the $fCO_{2\ (atm)}$ and 0.003 Pg C yr^{-1} for the sea ice uncertainty (Figure 5a, Figure S5 in Supporting Information S1). The $fCO_{2\ (atm)}$ component showed a ∼40% contribution from the $xCO_{2\ (atm)}$ uncertainty and a 60% relative contribution from the partial pressure of water vapor (pH_2O) component used in the calculation (Figure 5c). These components showed small increases following the increase in the absolute air-sea CO_2 flux (Figure 5d).

4. Discussion

4.1. Air-Sea CO_2 Flux and $fCO_{2\ (sw)}$ Uncertainties

Within this study, we present an air-sea CO_2 flux uncertainty budget for the fCO_2-product that builds on the principles of in situ Fiducial Reference Measurement (Banks et al., 2020), where all known sources of uncertainty are systematically considered (however small) and propagated to the final uncertainty using standard propagation techniques and a well-established uncertainty framework (BIPM, 2008; Taylor, 1997). Applying this approach has allowed the production of spatially and temporally complete air-sea CO_2 flux uncertainties. We showed in all cases that the $fCO_{2\ (sw)}$ uncertainties were the dominant source of uncertainty to the air-sea CO_2 flux when investigating individual locations and time points. This would indicate that when assessing variability or trends in the air-sea CO_2 fluxes, as a first step, the $fCO_{2\ (sw)}$ uncertainty should be accounted for within these assessments. For example, Ford et al. (2022b) calculated trends in the air-sea CO_2 fluxes in the South Atlantic Ocean and showed significant trends whilst accounting for the $fCO_{2\ (sw)}$ and gas transfer uncertainties. However, in this study in the South Atlantic Ocean, the wind speed uncertainty component was larger than the gas transfer uncertainty (Figure 4e, Figure S4 in Supporting Information S1), consistent with the results of Jersild and Landschützer (2024). Similarly in the Southern Ocean, the air and waterside solubility components were larger than both the gas transfer and wind speed uncertainties (Figure 4e). Therefore, it is important to assess all sources of uncertainties within the air-sea CO_2 fluxes as some components may be more dominant in some regions as opposed to others (Figure 4). These uncertainties should also be considered when assessing trends and/or more complex decompositions of seasonal, interannual and decadal variability (Ford et al., 2022b; Landschützer et al., 2016, 2018). A concerted effort to implement these full uncertainty budgets for the fCO_2-product based air-sea CO_2 fluxes in preparation for future advances and reductions of uncertainties in the air-sea CO_2 flux calculations would appear critical.

Within this air-sea CO_2 flux uncertainty budget, a spatially and temporally explicit approach to estimating the total $fCO_{2\ (sw)}$ uncertainty from an exemplar feed forward neural network approach (Landschützer et al., 2014;

Watson et al., 2020) was implemented (named UExP-FNN-U). Previous $fCO_{2\ (sw)}$ uncertainty estimates have assumed a fixed global value based on a comparison to the in situ SOCAT observations (Landschützer et al., 2013, 2014), which is equivalent to the evaluation uncertainty in this study. Our results show that in the subtropics, the use of the single fixed evaluation uncertainty may be applicable, as this was the dominant uncertainty within these regions. However, within more dynamic regions, such as the Arctic Ocean and Equatorial Pacific, the evaluation uncertainty will likely underestimate the total uncertainty due to the dominance of the network uncertainty within these regions. Some approaches have started to incorporate these further sources of uncertainty into their total $fCO_{2\ (sw)}$ uncertainty (Ford et al., 2022a) or consider only one of these $fCO_{2\ (sw)}$ components as their uncertainty (e.g., Chau et al., 2022). Therefore, these results would indicate a need to expand the current uncertainty estimation for globally resolved $fCO_{2\ (sw)}$ using the approach in this study as a framework.

Our study does present a seemingly counter intuitive result whereby the dynamic Southern Ocean, generally regarded as the one of the most under sampled regions, has lower total $fCO_{2\ (sw)}$ uncertainties than for example, the Equatorial Pacific (Figure 3b), a dynamic but more well sampled region. High frequency measurements are made within the Equatorial Pacific, for example, by the TOGA-TOA buoys that provide hourly data (Sutton et al., 2019). However, when these are gridded to monthly 1° regions, a lower number of 1° observations are produced within the province to constrain the neural network (i.e., see Figure S6 in Supporting Information S1 for the provinces). Comparing the provinces within the regions, we find that the Southern Ocean has twice as many available monthly 1° averaged observations to constrain the $fCO_{2\ (sw)}$ in comparison to the Equatorial Pacific. This situation therefore leads to the higher $fCO_{2\ (sw)}$ uncertainties in the Equatorial Pacific where the available data struggle to constrain the dynamic $fCO_{2\ (sw)}$ variability (Figure 3b). Although as shown in this study, the total air-sea CO_2 flux uncertainties are larger in the Southern Ocean (Figure 4a), leading to the higher uncertainty in estimating the Southern Ocean CO_2 uptake (e.g., Hauck, Gregor, et al., 2023).

Within the GCB, multiple fCO_2-products produce globally complete $fCO_{2\ (sw)}$ fields, which use different interpolation methodologies (Friedlingstein et al., 2023). These methods include neural networks (Chau et al., 2022; Landschützer et al., 2014; Watson et al., 2020), multi-linear regression (Iida et al., 2021) or other machine learning (Gloege et al., 2022) and interpolation (Rodenbeck et al., 2013) techniques, and therefore the basis of the three uncertainty components to the $fCO_{2\ (sw)}$ in this study can be adapted to equivalent uncertainties for these methodologies. For example, for a method that uses multi-regression, for example, (Iida et al., 2021) instead of a feed-forward neural network, the calculation of the evaluation uncertainty (i.e., comparison to the in situ SOCAT observations) would remain the same. The network uncertainty could be formed from either the standard deviation of multiple ensemble runs of the multi-linear regression (similar to the network uncertainty in this study) or could be constructed from the uncertainty in the linear regression fit parameters as the source of uncertainty. The parameter uncertainty would be similar to the approach in this study and would involve a Monte Carlo uncertainty propagation which propagates the input parameter uncertainties through the multi-linear regression. It is therefore clear that these uncertainties could be calculated for all fCO_2-products to produce spatially and temporally complete $fCO_{2\ (sw)}$ uncertainty fields for future GCB type analyses. This would be important as clearly the complete $fCO_{2\ (sw)}$ uncertainty fields form a key component in calculating spatially and temporally complete air-sea CO_2 flux.

4.2. Integrated Air-Sea CO_2 Flux Uncertainties

Within the GCB, the ocean carbon sink has been assessed by annually integrating the calculated air-sea CO_2 fluxes. The uncertainty on these estimates is assessed using literature values, and not all sources of uncertainty are evaluated within the assessment. In this study, we systematically assessed the components that contribute to the total air-sea CO_2 flux uncertainty and showed that these vary through time (Figures 5a and 5d). In this section, we discuss the uncertainty estimates (at the 1σ confidence) for the different components and compare them to the current GCB uncertainty estimate.

The GCB estimate for the $fCO_{2\ (sw)}$ mapping uncertainty is 0.20 Pg C yr^{-1} compared to the 0.48 Pg C yr^{-1} (Table 2) uncertainty identified in this study. The GCB estimate stems from Landschützer et al. (2014), where the uncertainty was estimated using the evaluation uncertainty of ∼12 µatm (1σ). As an example, applying a 12 µatm (1σ) evaluation uncertainty, and assuming the network and parameter uncertainties are 0, our methodology produces a mean 0.20 Pg C yr^{-1} uncertainty due to the $fCO_{2\ (sw)}$ between 1998 and 2010 (same period as Landschützer et al., 2014), so our calculation methods are consistent with that of the earlier Landschützer

et al. (2014) work. Since the initial work by Landschützer et al. (2014), the evaluation uncertainty for most data products has increased to around ~20 µatm (1σ; 22 µatm for the UExP-FNN-U; Figure S3c in Supporting Information S1) (Gregor et al., 2019). This increase in the evaluation uncertainty increases the $fCO_{2\ (sw)}$ evaluation uncertainty to a mean of 0.44 Pg C yr^{-1} between 1985 and 2022, but within this study we also consider the network (0.15 Pg C yr^{-1}) and parameter uncertainties (0.09 Pg C yr^{-1}). Chau et al. (2022) show an equivalent network uncertainty for their approach to be 0.13 Pg C yr^{-1}, consistent with this study. The three $fCO_{2\ (sw)}$ components in our study all contribute to a larger uncertainty of 0.48 Pg C yr^{-1} than that estimated by Landschützer et al. (2014) of 0.18 Pg C yr^{-1}.

The gas transfer uncertainty has been assessed at 0.20 Pg C yr^{-1} within the GCB, compared to the 0.47 Pg C yr^{-1} (Table 2) in this study. Woolf et al. (2019) suggest two representative values for the gas transfer uncertainty of 0.20 Pg C yr^{-1} (1σ assuming a 10% gas transfer uncertainty) or 0.40 Pg C yr^{-1} (1σ assuming a 20% gas transfer uncertainty). In this study, we estimate a slightly higher uncertainty than suggested by Woolf et al. (2019); however, our results indicate that this uncertainty was proportional to the absolute air-sea CO_2 flux (Figure 5d), which is feasible given the potential bias introduced by bubble-mediated transfer and related asymmetric transfer (Leighton et al., 2018). Although our result is higher than the current GCB estimate, it remains consistent if the 10% gas transfer uncertainty was selected. However, we propose the use of the 20% uncertainty as a conservative estimate for the gas transfer uncertainty, and that this component be calculated for each product based on the absolute air-sea CO_2 flux. Future work could expand the analysis to implement condition dependent uncertainties for gas exchange parameterizations if they were provided by the gas transfer community (e.g., uncertainties due to chemical enhancement at low wind speeds; Wanninkhof, 2014).

Recently, the evaluation of wind speed products has indicated that a 0.09 Pg C yr^{-1} (Fay et al., 2021; Roobaert et al., 2018) uncertainty stems from the wind speed uncertainty. We have shown a slightly smaller but still consistent value of 0.07 Pg C yr^{-1} (Table 2) using a different methodology. Fay et al. (2021) estimate the uncertainty as the standard deviation of the net CO_2 sink calculated using three different wind products, where the standard deviation may, with a small sample size, overestimate the full uncertainty within the wind products. Our results may also be slightly smaller due to the connection to the absolute air-sea CO_2 flux, which is likely different from the products used in the previous work.

The other components assessed in this study have not previously been investigated and are currently not included within the GCB estimates. The solubility components within this study introduce a 0.08 Pg C yr^{-1} uncertainty. The inclusion of two solubility terms within this study stems from the inclusion of vertical temperature gradients at the ocean's surface, as described by Woolf et al. (2016). The skin and subskin solubilities are calculated at slightly different temperatures and salinities (cool and salty skin), and therefore have subtly different values when integrated globally. Within the GCB, all the fCO_2-product based assessments, except for the UoEx-Watson, do not include the vertical temperature gradients (Friedlingstein et al., 2023) and therefore have a single solubility term. Although the evidence is growing for the inclusion of these temperature gradients (Bellenger et al., 2023; Dong et al., 2022, 2024; Shutler et al., 2020; Watson et al., 2020; Woolf et al., 2016), the use of a single or two solubilities does not have a large effect on the total combined uncertainty (i.e., 0.10 Pg C yr^{-1} for two solubilities, or 0.08 Pg C yr^{-1} for one solubility assuming the solubilities are independent and uncorrelated). In this study, we have assessed the precision of the air-sea CO_2 flux estimates, whereby the corrections for the vertical temperature gradients would represent biases in the air-sea CO_2 flux (affecting the accuracy) but would have little impact on the precision (Dong et al., 2022, 2024).

The sea ice component presents a very small uncertainty on the global scale of 0.003 Pg C yr^{-1}. The inclusion of sea ice within the air-sea CO_2 flux calculation assumes that the flux decreases linearly with increasing sea ice concentration (i.e., ice is a complete barrier to air-sea fluxes) (Arrigo & Van Dijken, 2007; Shutler et al., 2016; Takahashi et al., 2009). Although there remains a debate within sea ice communities as to the relationship between sea ice coverage and air-sea CO_2 fluxes. This is in part due to conflicting observations that fluxes can occur through sea ice (e.g., Geilfus et al., 2014) and whether sea ice inhibits (e.g., Prytherch & Yelland, 2021) or enhances (e.g., Kohout & Meylan, 2008) turbulence, thereby modifying the CO_2 flux (see discussion and references within Watts et al. (2022)). Additionally, the effect of sea ice melt creating shallow stratification that can modify the $fCO_{2\ (sw)}$ at the surface can introduce further uncertainties in these sea ice regions (e.g., Dong, Yang, Bakker, Liss, et al., 2021). These components will introduce further uncertainties into the sea ice component but

cannot currently be quantified. However, at the global scale, these uncertainties will remain small relative to the other components due to the small areal coverage but will likely increase on regional scales.

We have focussed our uncertainty analysis on the global scale; however, the principles and calculations applied globally are applicable to the regional scale. Within regional assessments the fixed components will remain of similar relative magnitudes. However, the spatially correlated components will increase in magnitude due to the calculated decorrelation lengths (i.e., as the region assessed gets smaller, the uncertainties within the region become more correlated and therefore larger when integrated). Previous GCB assessments have shown global agreement between the fCO_2-product based approaches within the uncertainties (Friedlingstein et al., 2022, 2023) but regional differences are still relatively large for example, (Fay & McKinley, 2021; Ford et al., 2022a; Friedlingstein et al., 2023). In future work, the application of the uncertainty framework in this study to regional air-sea CO_2 flux budgets will be an important step to improve future regional air-sea CO_2 flux budgets.

4.3. Uncertainty Estimates for the Global Carbon Budget

The GCB has identified that the fCO_2-products and models which assess the global ocean carbon sink have been slowly diverging, and are starting to diverge outside the current calculated uncertainty (see Figure 10 in Friedlingstein et al. (2023)). Hauck, Nissen et al. (2023) indicated that the ocean carbon sink uncertainty for the data products may be underestimated and suggested a value of 0.60 Pg C yr^{-1} before the riverine adjustment uncertainty was included. Within this study we show an updated mean uncertainty of 0.70 Pg C yr^{-1} between 1985 and 2022, before the riverine adjustment and in situ $fCO_{2\ (sw)}$ uncertainty were included. When the in situ $fCO_{2\ (sw)}$ uncertainty of 0.20 Pg C yr^{-1} (which can be calculated within the approach assuming a 2 µatm $fCO_{2\ (sw)}$ uncertainty that is correlated globally; Bakker et al., 2016) and river flux adjustment uncertainty of 0.15 Pg C yr^{-1} (0.30 Pg C yr^{-1} is the 2σ equivalent uncertainty; Regnier et al., 2022) are included, assuming these are independent and uncorrelated we estimate a GCB equivalent mean uncertainty for the UExP-FNN-U of 0.74 Pg C yr^{-1}. Although we have calculated a fixed value here which could be used within future GCB assessments, we strongly recommend that each data product be assessed to determine their own uncertainty budgets and then a full and temporally varying uncertainty budget for the GCB fCO_2-product ensemble can be derived. Our results have shown that the size and dominance of the different components vary through time, and some components show variability that follows the absolute air-sea CO_2 flux, which will be different for each product and will likely track atmospheric emissions. This study could be used as a framework to allow these uncertainties to be calculated for each data product for future releases of the GCB assessments. It would also appear critical to apply the same uncertainty framework principles (i.e., construct a systematic uncertainty budget) to alternative approaches to estimating the annual global ocean carbon sink, including the global biogeochemical models. All software for the analysis framework and the gas flux calculations are available as open-source (CC-BY license) and these are version controlled and fully traceable (Ford et al., 2024a).

5. Conclusions

In this study, we have presented a framework to estimate spatially and temporally varying air-sea CO_2 flux uncertainties, which systematically assessed all sources of uncertainties and was built upon standard uncertainty propagation methodologies and an established uncertainty approach. We show that when investigating single locations, $fCO_{2\ (sw)}$ was the dominant source of uncertainty for air-sea CO_2 fluxes. However, we show that the relative contributions by the remaining sources of uncertainty varied spatially, such that the gas transfer uncertainty was not always the second most dominant source of uncertainty. Within this, the $fCO_{2\ (sw)}$ uncertainties were estimated using a similar systematic uncertainty budget that considered three sources of uncertainties in an exemplar feed forward neural network scheme (the UExP-FNN-U). We show that the evaluation uncertainty (comparison to SOCAT in situ observations) was the largest source of uncertainty in the subtropics; however, the network uncertainty (uncertainty within the neural network ensemble) was dominant in some dynamic regions such as the Arctic Ocean. The parameter uncertainty (propagated input parameter uncertainties through the neural network) was a small contribution to the combined uncertainty.

The calculated air-sea CO_2 fluxes were integrated into annual estimates of the net air-sea CO_2 flux, or the ocean carbon sink, between 1985 and 2022 as commonly produced for the Global Carbon Budget assessments. We present an approach to integrate the calculated air-sea CO_2 flux uncertainties by providing temporally varying ocean carbon sink uncertainties. We showed a mean 1σ ocean carbon sink uncertainty between 1985 and 2022 of

0.70 Pg C yr^{-1}. Over this period, the $fCO_{2\ (sw)}$ component equated to a mean of 0.48 Pg C yr^{-1}, followed by the gas transfer at 0.47 Pg C yr^{-1}. The dominant component switched from the $fCO_{2\ (sw)}$ before ∼2010, to the gas transfer after ∼2010. Smaller sources of uncertainty included the wind speed uncertainty (0.07 Pg C yr^{-1}), solubility (0.08 Pg C yr^{-1}) and Schmidt number (0.06 Pg C yr^{-1}).

Finally, we provide a Global Carbon Budget equivalent mean 1σ uncertainty (i.e., including the riverine flux adjustment and in situ $fCO_{2\ (sw)}$ uncertainties) of 0.74 Pg C yr^{-1} for the UExP-FNN-U. This study provides an approach to estimating a complete air-sea CO_2 flux uncertainty budget that could be used by the community to provide time varying and consistent uncertainties for use within the Global Carbon Budget and other assessment studies.

Data Availability Statement

Input data sets used within this study are tabulated in Table S1 of the Supporting Information S1 with their respective DOIs. The software used within this study is available open source in Ford et al. (2024a), and updated at https://github.com/JamieLab/OceanICU. Output from the analysis in this study, including the input data sets on the 1° monthly grid, output from the UExP-FNN-U, air-sea CO_2 fluxes and their respective uncertainty components, can be downloaded from Ford et al. (2024b).

Acknowledgments
This work was funded by the Convex Seascape Survey (https://convexseascapesurvey.com/) and the European Union under grant agreement no. 101083922 (OceanICU; https://ocean-icu.eu/) and UK Research and Innovation (UKRI) under the UK government's Horizon Europe funding guarantee (Grants 10054454, 10063673, 10064020, 10059241, 10079684, 10059012, 10048179). The views, opinions and practices used to produce this data set/software are however those of the author(s) only and do not necessarily reflect those of the European Union or European Research Executive Agency. Neither the European Union nor the granting authority can be held responsible for them. The Surface Ocean CO_2 Atlas (SOCAT) is an international effort, endorsed by the International Ocean Carbon Coordination Project (IOCCP), the Surface Ocean Lower Atmosphere Study (SOLAS) and the Integrated Marine Biosphere Research (IMBeR) program, to deliver a uniformly quality-controlled surface ocean CO_2 database. Many researchers and funding agencies responsible for the collection of data and quality control are thanked for their contributions to SOCAT. For the purpose of open access, the authors has applied a Creative Commons Attribution (CC BY) licence to any Author Accepted Manuscript version arising from this submission.

References

Amari, S. I., Murata, N., Müller, K. R., Finke, M., & Yang, H. H. (1997). Asymptotic statistical theory of overtraining and cross-validation. *IEEE Transactions on Neural Networks*, *8*(5), 985–996. https://doi.org/10.1109/72.623200

Arrigo, K. R., & Van Dijken, G. L. (2007). Interannual variation in air-sea CO_2 flux in the Ross Sea, Antarctica: A model analysis. *Journal of Geophysical Research*, *112*(C3), 2006JC003492. https://doi.org/10.1029/2006JC003492

Bakker, D. C. E., Pfeil, B., Landa, C. S., Metzl, N., O'Brien, K. M., Olsen, A., et al. (2016). A multi-decade record of high-quality fCO_2 data in version 3 of the Surface Ocean CO_2 Atlas (SOCAT). *Earth System Science Data*, *8*(2), 383–413. https://doi.org/10.5194/essd-8-383-2016

Banks, A. C., Vendt, R., Alikas, K., Bialek, A., Kuusk, J., Lerebourg, C., et al. (2020). Fiducial reference measurements for satellite ocean colour (FRM4SOC). *Remote Sensing*, *12*(8), 1322. https://doi.org/10.3390/RS12081322

Bellenger, H., Bopp, L., Ethé, C., Ho, D., Duvel, J. P., Flavoni, S., et al. (2023). Sensitivity of the global ocean carbon sink to the ocean skin in a climate model. *Journal of Geophysical Research: Oceans*, *128*(7), e2022JC019479. https://doi.org/10.1029/2022JC019479

BIPM. (2008). Evaluation of measurement data—Guide to the expression of uncertainty in measurement.

Chau, T. T. T., Gehlen, M., & Chevallier, F. (2022). A seamless ensemble-based reconstruction of surface ocean CO_2 and air–sea CO_2 fluxes over the global coastal and open oceans. *Biogeosciences*, *19*(4), 1087–1109. https://doi.org/10.5194/bg-19-1087-2022

Chen, Z., Suntharalingam, P., Watson, A. J., Schuster, U., Zhu, J., & Zeng, N. (2021). Variability of North Atlantic CO_2 fluxes for the 2000–2017 period estimated from atmospheric inverse analyses. *Biogeosciences*, *18*(15), 4549–4570. https://doi.org/10.5194/bg-18-4549-2021

Demuth, H., Beale, M., & Hagan, M. (2008). *Neural network toolbox 6 users guide*. The MathWorks, Inc. 3 Apple Hill Drive.

Dong, Y., Bakker, D. C. E., Bell, T. G., Huang, B., Landschützer, P., Liss, P. S., & Yang, M. (2022). Update on the temperature corrections of global air-sea CO_2 flux estimates. *Global Biogeochemical Cycles*, *36*(9). https://doi.org/10.1029/2022GB007360

Dong, Y., Bakker, D. C. E., Bell, T. G., Yang, M., Landschützer, P., Hauck, J., et al. (2024). Direct observational evidence of strong CO_2 uptake in the Southern Ocean. *Science Advances*, *10*(30), eadn5781. https://doi.org/10.1126/sciadv.adn5781

Dong, Y., Yang, M., Bakker, D. C. E., Kitidis, V., & Bell, T. G. (2021). Uncertainties in eddy covariance air–sea CO_2 flux measurements and implications for gas transfer velocity parameterisations. *Atmospheric Chemistry and Physics*, *21*(10), 8089–8110. https://doi.org/10.5194/acp-21-8089-2021

Dong, Y., Yang, M., Bakker, D. C. E., Liss, P. S., Kitidis, V., Brown, I., et al. (2021). Near-surface stratification due to ice melt biases Arctic air-sea CO_2 flux estimates. *Geophysical Research Letters*, *48*(22), e2021GL095266. https://doi.org/10.1029/2021GL095266

Edson, J. B., Jampana, V., Weller, R. A., Bigorre, S. P., Plueddemann, A. J., Fairall, C. W., et al. (2013). On the exchange of momentum over the open ocean. *Journal of Physical Oceanography*, *43*(8), 1589–1610. https://doi.org/10.1175/JPO-D-12-0173.1

Fairall, C. W., Bradley, E. F., Godfrey, J. S., Wick, G. A., Edson, J. B., & Young, G. S. (1996). Cool-skin and warm-layer effects on sea surface temperature. *Journal of Geophysical Research*, *101*(C1), 1295–1308. https://doi.org/10.1029/95JC03190

Fay, A. R., Gregor, L., Landschützer, P., McKinley, G. A., Gruber, N., Gehlen, M., et al. (2021). SeaFlux: Harmonization of air–sea CO_2 fluxes from surface CO_2 data products using a standardized approach. *Earth System Science Data*, *13*(10), 4693–4710. https://doi.org/10.5194/essd-13-4693-2021

Fay, A. R., & McKinley, G. A. (2021). Observed regional fluxes to constrain modeled estimates of the ocean carbon sink. *Geophysical Research Letters*, *48*(20), e2021GL095325. https://doi.org/10.1029/2021GL095325

Ford, D. J., Blannin, J., Watts, J., Watson, A. J., Landschutzer, P., Jersild, A., & Shutler, J. D. (2024a). OceanICU Neural Network Framework with per pixel uncertainty propagation (v1.1) (version v1.1). *Zenodo*. https://doi.org/10.5281/ZENODO.12597803

Ford, D. J., Blannin, J., Watts, J., Watson, A. J., Landschutzer, P., Jersild, A., & Shutler, J. D. (2024b). Data supporting "A comprehensive analysis of air-sea CO2 flux uncertainties constructed from surface ocean data products" [Dataset]. *Zenodo*. https://doi.org/10.5281/zenodo.13911533

Ford, D. J., Sims, R. P., Shutler, J. D., Ashton, I., & Holding, T. (2023). Reanalysed (depth and temperature consistent) surface ocean CO_2 atlas (SOCAT) version 2023 (version 2023-0) [Dataset]. *Zenodo*. https://doi.org/10.5281/ZENODO.8229316

Ford, D. J., Tilstone, G. H., Shutler, J. D., & Kitidis, V. (2022a). Derivation of seawater pCO_2 from net community production identifies the South Atlantic Ocean as a CO_2 source. *Biogeosciences*, *19*(1), 93–115. https://doi.org/10.5194/bg-19-93-2022

Ford, D. J., Tilstone, G. H., Shutler, J. D., & Kitidis, V. (2022b). Identifying the biological control of the annual and multi-year variations in South Atlantic air–sea CO_2 flux. *Biogeosciences*, *19*(17), 4287–4304. https://doi.org/10.5194/bg-19-4287-2022

Ford, D. J., Tilstone, G. H., Shutler, J. D., Kitidis, V., Lobanova, P., Schwarz, J., et al. (2021). Wind speed and mesoscale features drive net autotrophy in the South Atlantic Ocean. *Remote Sensing of Environment*, *260*, 112435. https://doi.org/10.1016/j.rse.2021.112435

Friedlingstein, P., O'Sullivan, M., Jones, M. W., Andrew, R. M., Bakker, D. C. E., Hauck, J., et al. (2023). Global carbon budget 2023. *Earth System Science Data*, *15*(12), 5301–5369. https://doi.org/10.5194/essd-15-5301-2023

Friedlingstein, P., O'Sullivan, M., Jones, M. W., Andrew, R. M., Gregor, L., Hauck, J., et al. (2022). Global carbon budget 2022. *Earth System Science Data*, *14*(11), 4811–4900. https://doi.org/10.5194/essd-14-4811-2022

GEBCO Bathymetric Compilation Group. (2023). *The GEBCO_2023 grid—A continuous terrain model of the global oceans and land. (Version 1) [Documents, Network Common Data Form]*. NERC EDS British Oceanographic Data Centre NOC. https://doi.org/10.5285/F98B053B-0CBC-6C23-E053-6C86ABC0AF7B

Geilfus, N.-X., Tison, J.-L., Ackley, S. F., Galley, R. J., Rysgaard, S., Miller, L. A., & Delille, B. (2014). Sea ice CO_2 dynamics and air–ice CO_2 fluxes during the Sea Ice Mass Balance in the Antarctic (SIMBA) experiment—Bellingshausen Sea, Antarctica. *The Cryosphere*, *8*(6), 2395–2407. https://doi.org/10.5194/tc-8-2395-2014

Gloege, L., Yan, M., Zheng, T., & McKinley, G. A. (2022). Improved quantification of ocean carbon uptake by using machine learning to merge global models and pCO_2 data. *Journal of Advances in Modeling Earth Systems*, *14*(2), e2021MS002620. https://doi.org/10.1029/2021MS002620

Gregor, L., & Gruber, N. (2021). OceanSODA-ETHZ: A global gridded data set of the surface ocean carbonate system for seasonal to decadal studies of ocean acidification. *Earth System Science Data*, *13*(2), 777–808. https://doi.org/10.5194/essd-13-777-2021

Gregor, L., Lebehot, A. D., Kok, S., & Scheel Monteiro, P. M. (2019). A comparative assessment of the uncertainties of global surface ocean CO_2 estimates using a machine-learning ensemble (CSIR-ML6 version 2019a)-Have we hit the wall? *Geoscientific Model Development*, *12*(12), 5113–5136. https://doi.org/10.5194/gmd-12-5113-2019

Hauck, J., Gregor, L., Nissen, C., Patara, L., Hague, M., Mongwe, P., et al. (2023). The southern ocean carbon cycle 1985–2018: Mean, seasonal cycle, trends, and storage. *Global Biogeochemical Cycles*, *37*(11), e2023GB007848. https://doi.org/10.1029/2023GB007848

Hauck, J., Landschützer, P., Mayot, N., & Jersild, A. (2023). Global carbon budget 2023, surface ocean fugacity of CO_2 (fCO_2) and air-sea CO_2 flux of individual global ocean biogechemical models and surface ocean fCO_2-based data-products [Dataset]. *Zenodo*. https://doi.org/10.5281/ZENODO.10222484

Hauck, J., Nissen, C., Landschützer, P., Rödenbeck, C., Bushinsky, S., & Olsen, A. (2023). Sparse observations induce large biases in estimates of the global ocean CO_2 sink: An ocean model subsampling experiment. *Philosophical Transactions of the Royal Society A: Mathematical, Physical & Engineering Sciences*, *381*(2249), 20220063. https://doi.org/10.1098/rsta.2022.0063

Hersbach, H., Bell, B., Berrisford, P., Biavati, G., Horányi, A., Muñoz Sabater, J., et al. (2019). ERA5 monthly averaged data on single levels from 1979 to present [Dataset]. *Copernicus Climate Change Service (C3S) Climate Data Store (CDS)*. https://doi.org/10.24381/cds.f17050d7

Ho, D. T., Wanninkhof, R., Schlosser, P., Ullman, D. S., Hebert, D., & Sullivan, K. F. (2011). Toward a universal relationship between wind speed and gas exchange: Gas transfer velocities measured with $^3He/SF_6$ during the Southern Ocean Gas Exchange Experiment. *Journal of Geophysical Research*, *116*, C00F04. https://doi.org/10.1029/2010JC006854

Holding, T., Ashton, I. G., Shutler, J. D., Land, P. E., Nightingale, P. D., Rees, A. P., et al. (2019). The FluxEngine air–sea gas flux toolbox: Simplified interface and extensions for in situ analyses and multiple sparingly soluble gases. *Ocean Science*, *15*(6), 1707–1728. https://doi.org/10.5194/os-15-1707-2019

Iida, Y., Takatani, Y., Kojima, A., & Ishii, M. (2021). Global trends of ocean CO_2 sink and ocean acidification: An observation-based reconstruction of surface ocean inorganic carbon variables. *Journal of Oceanography*, *77*(2), 323–358. https://doi.org/10.1007/s10872-020-00571-5

Jähne, B., Huber, W., Dutzi, A., Wais, T., & Ilmberger, J. (1984). Wind/wave-tunnel experiment on the Schmidt number—And wave field dependence of air/water gas exchange. In W. Brutsaert, & G. H. Jirka (Eds.), *Gas transfer at water surfaces* (pp. 303–309). Springer Netherlands. https://doi.org/10.1007/978-94-017-1660-4_28

Jean-Michel, L., Eric, G., Romain, B.-B., Gilles, G., Angélique, M., Marie, D., et al. (2021). The Copernicus global 1/12° oceanic and sea ice GLORYS12 reanalysis. *Frontiers in Earth Science*, *9*(July), 1–27. https://doi.org/10.3389/feart.2021.698876

Jersild, A., & Landschützer, P. (2024). A spatially explicit uncertainty analysis of the air-sea CO_2 flux from observations. *Geophysical Research Letters*, *51*(4), e2023GL106636. https://doi.org/10.1029/2023GL106636

Kern, S. (2021). Spatial correlation length scales of sea-ice concentration errors for high-concentration pack ice. *Remote Sensing*, *13*(21), 4421. https://doi.org/10.3390/rs13214421

Kohout, A. L., & Meylan, M. H. (2008). An elastic plate model for wave attenuation and ice floe breaking in the marginal ice zone. *Journal of Geophysical Research*, *113*(C9), 2007JC004434. https://doi.org/10.1029/2007JC004434

Lan, X., Tans, P., & Thoning, K., & NOAA Global Monitoring Laboratory. (2023). NOAA greenhouse gas marine boundary layer reference—CO_2 [Dataset]. *NOAA GML*. https://doi.org/10.15138/DVNP-F961

Landschützer, P., Gruber, N., & Bakker, D. C. E. (2016). Decadal variations and trends of the global ocean carbon sink. *Global Biogeochemical Cycles*, *30*(10), 1396–1417. https://doi.org/10.1002/2015GB005359

Landschützer, P., Gruber, N., Bakker, D. C. E., & Schuster, U. (2014). Recent variability of the global ocean carbon sink. *Global Biogeochemical Cycles*, *28*(9), 927–949. https://doi.org/10.1002/2014GB004853

Landschützer, P., Gruber, N., Bakker, D. C. E., Schuster, U., Nakaoka, S., Payne, M. R., et al. (2013). A neural network-based estimate of the seasonal to inter-annual variability of the Atlantic Ocean carbon sink. *Biogeosciences*, *10*(11), 7793–7815. https://doi.org/10.5194/bg-10-7793-2013

Landschützer, P., Gruber, N., Bakker, D. C. E., Stemmler, I., & Six, K. D. (2018). Strengthening seasonal marine CO_2 variations due to increasing atmospheric CO_2. *Nature Climate Change*, *8*(2), 146–150. https://doi.org/10.1038/s41558-017-0057-x

Leighton, T. G., Coles, D. G. H., Srokosz, M., White, P. R., & Woolf, D. K. (2018). Asymmetric transfer of CO_2 across a broken sea surface. *Scientific Reports*, *8*(1), 8301. https://doi.org/10.1038/s41598-018-25818-6

Longhurst, A. (1998). *Ecological geography of the sea*. Academic Press.

Ludovic, B., Byron, B., Fairall, C., Thompson, E., Jim, E., & Pincus, R. (2021). Python implementation of the COARE 3.5 bulk air-sea flux algorithm (version v1.1). *Zenodo*. https://doi.org/10.5281/ZENODO.5110991

Mälicke, M. (2022). SciKit-GStat 1.0: A SciPy-flavored geostatistical variogram estimation toolbox written in Python. *Geoscientific Model Development*, *15*(6), 2505–2532. https://doi.org/10.5194/gmd-15-2505-2022

Mears, C., Lee, T., Ricciardulli, L., Wang, X., & Wentz, F. (2022a). Improving the accuracy of the cross-calibrated multi-platform (CCMP) ocean vector winds. *Remote Sensing*, *14*(17), 4230. https://doi.org/10.3390/rs14174230

Mears, C., Lee, T., Ricciardulli, L., Wang, X., & Wentz, F. (2022b). RSS Cross-Calibrated Multi-Platform (CCMP) monthly ocean vector wind analysis on 0.25 deg grid, version 3.0 [Dataset]. *Remote Sensing Systems (RSS) Air-Sea Essential Climate Variables (AS-ECV)*. https://doi.org/10.56236/RSS-uv1m30

Merchant, C. J., Embury, O., Bulgin, C. E., Block, T., Corlett, G. K., Fiedler, E., et al. (2019). Satellite-based time-series of sea-surface temperature since 1981 for climate applications. *Scientific Data*, *6*(1), 223. https://doi.org/10.1038/s41597-019-0236-x

Nightingale, P. D., Malin, G., Law, C. S., Watson, A. J., Liss, P. S., Liddicoat, M. I., et al. (2000). In situ evaluation of air-sea gas exchange parameterizations using novel conservative and volatile tracers. *Global Biogeochemical Cycles*, *14*(1), 373–387. https://doi.org/10.1029/1999GB900091

OSI SAF (2022). Global sea ice concentration climate data record v3.0—Multimission (version 3) [netCDF4]. *OSI SAF*. https://doi.org/10.15770/EUM_SAF_OSI_0013

Prytherch, J., & Yelland, M. J. (2021). Wind, convection and fetch dependence of gas transfer velocity in an Arctic sea-ice lead determined from eddy covariance CO_2 flux measurements. *Global Biogeochemical Cycles*, *35*(2), e2020GB006633. https://doi.org/10.1029/2020GB006633

Regnier, P., Resplandy, L., Najjar, R. G., & Ciais, P. (2022). The land-to-ocean loops of the global carbon cycle. *Nature*, *603*(7901), 401–410. https://doi.org/10.1038/s41586-021-04339-9

Rodenbeck, C., Keeling, R. F., Bakker, D. C. E., Metzl, N., Olsen, A., Sabine, C., & Heimann, M. (2013). Global surface-ocean pCO_2 and sea—Air CO_2 flux variability from an observation-driven ocean mixed-layer scheme. *Ocean Science*, *9*(2), 193–216. https://doi.org/10.5194/os-9-193-2013

Roobaert, A., Laruelle, G. G., Landschützer, P., & Regnier, P. (2018). Uncertainty in the global oceanic CO_2 uptake induced by wind forcing: Quantification and spatial analysis. *Biogeosciences*, *15*(6), 1701–1720. https://doi.org/10.5194/bg-15-1701-2018

Shutler, J. D., Gruber, N., Findlay, H. S., Land, P. E., Gregor, L., Holding, T., et al. (2024). The increasing importance of satellite observations to assess the ocean carbon sink and ocean acidification. *Earth-Science Reviews*, *250*, 104682. https://doi.org/10.1016/j.earscirev.2024.104682

Shutler, J. D., Land, P. E., Piolle, J. F., Woolf, D. K., Goddijn-Murphy, L., Paul, F., et al. (2016). FluxEngine: A flexible processing system for calculating atmosphere-ocean carbon dioxide gas fluxes and climatologies. *Journal of Atmospheric and Oceanic Technology*, *33*(4), 741–756. https://doi.org/10.1175/JTECH-D-14-00204.1

Shutler, J. D., Wanninkhof, R., Nightingale, P. D., Woolf, D. K., Bakker, D. C., Watson, A., et al. (2020). Satellites will address critical science priorities for quantifying ocean carbon. *Frontiers in Ecology and the Environment*, *18*(1), 27–35. https://doi.org/10.1002/fee.2129

Sutton, A. J., Feely, R. A., Maenner-Jones, S., Musielwicz, S., Osborne, J., Dietrich, C., et al. (2019). Autonomous seawater CO_2 and pH time series from 40 surface buoys and the emergence of anthropogenic trends. *Earth System Science Data*, *11*(1), 421–439. https://doi.org/10.5194/essd-11-421-2019

Takahashi, T., Sutherland, S. C., Wanninkhof, R., Sweeney, C., Feely, R. A., Chipman, D. W., et al. (2009). Climatological mean and decadal change in surface ocean pCO_2, and net sea-air CO_2 flux over the global oceans. *Deep-Sea Research Part II Topical Studies in Oceanography*, *56*(8–10), 554–577. https://doi.org/10.1016/j.dsr2.2008.12.009

Taylor, J. R. (1997). *An introduction to error analysis*. University Science Books.

Wanninkhof, R. (2014). Relationship between wind speed and gas exchange over the ocean revisited. *Limnology and Oceanography: Methods*, *12*(JUN), 351–362. https://doi.org/10.4319/lom.2014.12.351

Wanninkhof, R., Park, G. H., Takahashi, T., Sweeney, C., Feely, R., Nojiri, Y., et al. (2013). Global ocean carbon uptake: Magnitude, variability and trends. *Biogeosciences*, *10*(3), 1983–2000. https://doi.org/10.5194/bg-10-1983-2013

Watson, A. J., Schuster, U., Bakker, D. C. E., Bates, N. R., Corbière, A., González-Dávila, M., et al. (2009). Tracking the variable North Atlantic sink for atmospheric CO_2. *Science*, *326*(5958), 1391–1393. https://doi.org/10.1126/science.1177394

Watson, A. J., Schuster, U., Shutler, J. D., Holding, T., Ashton, I. G. C., Landschützer, P., et al. (2020). Revised estimates of ocean-atmosphere CO_2 flux are consistent with ocean carbon inventory. *Nature Communications*, *11*(1), 1–6. https://doi.org/10.1038/s41467-020-18203-3

Watts, J., Bell, T. G., Anderson, K., Butterworth, B. J., Miller, S., Else, B., & Shutler, J. (2022). Impact of sea ice on air-sea CO_2 exchange—A critical review of polar eddy covariance studies. *Progress in Oceanography*, *201*, 102741. https://doi.org/10.1016/j.pocean.2022.102741

Weiss, R. F. (1974). Carbon dioxide in water and seawater: The solubility of a non-ideal gas. *Marine Chemistry*, *2*(3), 203–215. https://doi.org/10.1016/0304-4203(74)90015-2

Weiss, R. F., & Price, B. A. (1980). Nitrous oxide solubility in water and seawater. *Marine Chemistry*, *8*(4), 347–359. https://doi.org/10.1016/0304-4203(80)90024-9

Woolf, D. K., Land, P. E., Shutler, J. D., Goddijn-Murphy, L. M., & Donlon, C. J. (2016). On the calculation of air-sea fluxes of CO_2 in the presence of temperature and salinity gradients. *Journal of Geophysical Research: Oceans*, *121*(2), 1229–1248. https://doi.org/10.1002/2015JC011427

Woolf, D. K., Shutler, J. D., Goddijn-Murphy, L., Watson, A. J., Chapron, B., Nightingale, P. D., et al. (2019). Key uncertainties in the recent air-sea flux of CO_2. *Global Biogeochemical Cycles*, *33*(12), 1548–1563. https://doi.org/10.1029/2018GB006041

References From the Supporting Information

CMEMS. (2021). Copernicus Marine Modelling Service global ocean physics reanalysis product (GLORYS12V1) [Dataset]. *Copernicus Marine Modelling Service*. https://doi.org/10.48670/moi-00021

Good, S. A., Embury, O., Bulgin, C. E., & Mittaz, J. (2019). ESA sea surface temperature climate change initiative (SST_cci): Level 4 analysis climate data record, version 2.1 [Dataset]. *Centre for Environmental Data Analysis (CEDA)*. https://doi.org/10.5285/62C0F97B1EAC4E0197A674870AFE1EE6